

Particulate organic matter dynamics and its isotopic signatures ($\delta^{13}\text{C}_{\text{POC}}$ and $\delta^{15}\text{N}_{\text{PN}}$) in relation to physical forcing in the central Arabian Sea during SW monsoon (2017-2018)

Saumya Silori^{1#}, Diksha Sharma^{1##}, *Mintu Chowdhury^{1###}, Haimanti Biswas^{1*}, Damien Cardinal², M. Mandeng-Yogo²

¹CSIR National Institute of Oceanography, Biological Oceanography Division,
Dona Paula, Goa 403004, India

²Laboratoire d'Océanographie et du Climat: Expérimentations et Approches Numériques
(LOCEAN-IPSL, Sorbonne Université, IRD, CNRS, MNHN) 4 Place Jussieu, 75005 Paris, France

*corresponding author: haimanti.biswas@nio.org; haimanti.biswas.nio@gmail.com

[#]Enrolled for Ph.D. Program (Aug 2016 - Aug 2021) under the Academy of Scientific and Innovative Research (AcSIR), Ghaziabad, 201002

^{##}Enrolled for Ph.D. under Bharthidasan University, Tiruchirappalli, TN, 620024

^{###}Affiliated for Ph.D., School of Oceanographic Studies, Jadavpur University, 188 Raja S.C. Mallick Rd, Kolkata 700032

Abstract

Monsoonal changes in particulate organic matter (POM) and its isotopic signatures ($\delta^{13}\text{C}_{\text{POC}}$ and $\delta^{15}\text{N}_{\text{PN}}$) were studied (Aug 2017 and 2018) in the central Arabian Sea (21-11°N 64°E). A low-level atmospheric jet (Findlater Jet) forms during the south-west (SW) monsoon and results in “open ocean upwelling” to the north of the jet’s axis. Higher wind speed and jet-induced wind stress curl coupled with low sea surface temperature (SST) and higher nutrients were noticed in 2018 than in 2017. The region to the north of the jet was characterized by substantially shallower Mixed Layers Depths (MLDs) and higher POM contents relative to the jet’s axis and southern stations. The molar ratio between particulate organic carbon (POC) and nitrogen (PN) (6.2 ± 1.9 in 2017; 6.4 ± 0.9 in 2018) was very close to the canonical Redfield ratio (6.63). The $\delta^{13}\text{C}_{\text{POC}}$ values (-26.3 ± 1.4 ‰ in 2017; 25.5 ± 1.4 ‰ in 2018) exhibited typical marine signature reported from this area and revealed a noticeable inter-annual difference. Relatively higher $\delta^{15}\text{N}_{\text{PN}}$ values noticed in the north (7.68 ± 2.6 ‰ in 2017; 9.24 ± 3 ‰ in 2018) indicated regenerated dissolved inorganic nitrogen coming from the oxygen minimum zone (OMZ) into the well-lit zone. The lower $\delta^{15}\text{N}_{\text{PN}}$ values along the jet axis and south of it were attributed to lateral advection of nitrogen from the Somali upwelling. Despite the higher nutrient availability, POC contents in 2018 did not exceed the values in 2017. Considering the total consumption of nitrogen (according to C:N: P=106:16:1), the potential POC development in 2018 could be double the value in 2017. The interannual differences in SW monsoon onset and wind speed seem to directly control the nutrient supply, affecting plankton community structure and POM variability. Thus, any future change in the physical forcing may directly influence the POC pool and consequent export flux to the mesopelagic.

Keywords: Central Arabian Sea; SW Monsoon; POC; $\delta^{13}\text{C}_{\text{POC}}$; PN, $\delta^{15}\text{N}_{\text{PN}}$; Phytoplankton; Upwelling.

1. Introduction

The Arabian Sea, a natural laboratory to study the bio-physical coupling, experiences a semi-annual reversal in the surface circulation mostly associated with seasonally changing winds generating northeast and south-west monsoons in winter and summer, respectively (Bauer et al., 1991). Both monsoons act differently to enhance vertical mixing and result in the entrainment of nutrient-rich deeper waters into the euphotic zone yielding high productivity (Banse, 1987). SW monsoon (June–September) is characterized by a strong low-level southwesterly jet (Findlater Jet) blowing across the basin, parallel to the coast of Oman (Findlater, 1977). The positive wind-stress curl to the northwest of the jet's axis drives open-ocean upwelling, whereas the negative wind-stress curl in the south-west results in downward Ekman pumping and consequently deeper mixed layers (Burkill et al., 1993; Smith & Bottero, 1977). The strong alongshore winds favor upwelling along the coast of Oman and Somalia. Several studies have noted the eastward advection of these upwelled waters off Oman's shelf (Young & Kindle, 1994; Mc Creary et al., 1996). Accordingly, the open-ocean upwelling and eastward advection of the upwelled waters support high productivity in the central Arabian Sea during the SW monsoon (Banse, 1987; Prasannakumar et al., 2000).

Very high particle flux accounting for nearly $1.3 - 3.3 \text{ g C m}^{-2} \text{ y}^{-1}$ was reported from this basin and is one of the highest recorded among the other tropical and subtropical basins (Haake et al. 1992). Previous sediment trap studies have demonstrated the monsoons' influence on the particle flux in the Arabian Sea (Nair et al., 1989; Haake et al., 1993; Rixen et al., 1996) with substantially higher fluxes during the SW monsoons (Rixen et al., 2005). A strong correlation between the particle flux and the strength of the SW monsoon, characterized by wind speeds, sea surface temperature (SST), and upwelling, suggests a close link between the surface processes and deeper waters (Haake et al., 1993; Rixen et al. 1997). The occurrence of diatom rich (identified by opal content) organic carbon in the sediment trap samples, particularly during the second phase of the SW monsoon (Aug), suggests that nutrient enrichment induces diatom bloom in the northern and central Arabian Sea which results in high POC export flux (Rixen et al. 2019). Calcifying phytoplankton like coccolithophore also contribute significantly to POC export and is noticed before the opal-dominated flux (Rixen et al. 2005). This suggests that the change in the phytoplankton community induced by any factor will directly impact the carbon export flux.

High productivity due to monsoonal forcing and poor ventilation of the mesopelagic waters in the Arabian Sea result in the formation of one of the most prominent Oxygen Minimum Zones (OMZs) between 150-1000 m (Banse et al., 2014; Rixen et al., 2020). The southward extension of this OMZ is seen till 9°N during the SW monsoon, whereas it moves up to 11°N during the NE monsoon (Shenoy

et al. 2020). The water column structure in the eastern and central Arabian Sea facilitates the reducing conditions, while oxygen deficiency is absent in the western and northwestern Arabian Sea (Naqvi, 1990). The peculiarity of OMZs dramatically modifies carbon and nitrogen biogeochemical cycles in the water column compared to the rest of the open ocean. Both Dissolved and Particulate Organic Carbon (DOC and POC) support the existence of the OMZ and associated denitrification in the Arabian Sea (Shetye et al., 2020). Phytoplankton-produced POC is the chief carbon source for the pelagic food web and is exported from the surface to deeper waters where it can be trapped for an extended period (century to millenia), a process known as the biological carbon pump (Le Moigne, 2019; Kharbush et al., 2020). Phytoplankton, bacteria, zooplankton, and detritus contribute to POC in varying percentages. Such relative contributions change seasonally and may have a direct impact on the POC sinking potential (Gauns et al., 2005). To evaluate the biogeochemical functioning of the Arabian Sea OMZ, $\delta^{15}\text{N}$ values of the particulate matter ($\delta^{15}\text{N}_{\text{PN}}$) can be employed to understand the relative contributions of deeper and laterally advected waters in supplying nitrogen to the euphotic zone. Arabian Sea OMZ is an important place for massive nitrogen loss due to strong denitrification (Sarkar et al., 2019), which discriminates ($\approx 20\text{-}30\text{‰}$) significantly amongst the stable isotopes of nitrogen (Voss et al., 2001). In the open-ocean regions, denitrification and nitrogen-fixation are the significant pathways having long-term controls on the isotopic composition of NO_3^- (Brandes & Devol, 2002). The process of denitrification converts NO_3^- to N_2 with strong discrimination against ^{15}N , which increases the $\delta^{15}\text{NO}_3^-$ values of the remaining NO_3^- in the water column, and the subsequent uptake of this ^{15}N enriched NO_3^- can propagate the isotopic signal to the POM (Voss et al., 2001). Based on this concept, we have tried to interlink the sources of nitrogen (from OMZ or lateral advection) to the euphotic zone and consequent POM development. While there are few nitrogen isotopic studies on $\delta^{15}\text{N}$ of N_2 , NO_3^- , N_2O and particulate matter from the Arabian sea (Naqvi et al., 1998; Montoya et al., 2006; Naqvi et al., 2006), such a hypothesis has not been explored in this region.

Similarly, the trends in $\delta^{13}\text{C}_{\text{POC}}$ have not been reported yet. Factors such as sources or availability of carbon, phytoplankton community composition and growth rate, nutrient, light availability, and microbial respiration may affect isotopic fractionation and lead to distinct trends in $\delta^{13}\text{C}_{\text{POC}}$ values (Hinga et al., 1994; Silori et al., 2021 and the references therein).

Considering such gap, the present study aims to elucidate the variations in POM dynamics driven by the interannual changes in the progression and strength of the SW monsoon. In this context, we investigated the variations in the POC, PN, $\delta^{13}\text{C}_{\text{POC}}$, and $\delta^{15}\text{N}_{\text{PN}}$ in the upper water column during two subsequent SW monsoon cruises to interlink the factors governing POM variability and consequent particle flux.

2. Materials and Methods

2.1 Sample Collection and Analysis

Two cruises were undertaken onboard RV Sindhu Sadhna from 3rd to 28th Aug 2017 (SSD 040) and from 2nd to 31st Aug 2018 (SSD 055) along the central (64°E) Arabian Sea (AS) (Fig 1). The Southwest monsoon 2017 and 2018 will be addressed as SWM-17 and SWM-18, respectively in the text. Sampling covered 11 stations from 21°N to 11°N at an interval of 1°, we could not sample 19°N station during 2017 due to extreme weather conditions. A CTD (Seabird, USA) fitted to the rosette system with 24, 10L Niskin bottles were used for the depth sampling at every station. Temperature, salinity and fluorescence values were obtained from the CTD sensors. The MLD was calculated using a 0.2 kg m⁻³ density difference from the surface (Gupta et al., 2016).

Water samples for dissolved oxygen (DO) and dissolved inorganic nutrients were collected from surface, 5, 10, 20, 30, 40, 50, 60, 80, 100, and 120 m depths. The Winkler method was used to analyse DO. The samples were immediately fixed after collection with Winkler reagents (A+B), and the brown precipitate was allowed to settle to one-third of the bottle's volume. The precipitate was dissolved by adding 1:1 H₂SO₄ followed by titration against pre-calibrated thiosulphate solution within 3-4 hours of collection (Winkler, 1888). Duplicate samples for dissolved inorganic nitrogen (nitrite, nitrate+nitrite = DIN), dissolved silicate (DSi), and dissolved inorganic phosphate (DIP) were collected from the aforementioned depths and analyzed onboard immediately after collection. The standard colorimetric method (UV-1800 UV-Vis Spectrophotometer, Shimadzu) by Grasshoff et al. (1992) was utilized to measure the concentrations of nitrate, nitrite, and silicate against the standard reference solutions (K₂HPO₄, Na₂SiF₆, and KNO₃(Sigma)). Dissolved inorganic phosphate was measured following the UNESCO (1983) method.

The samples for POC, PN quantification, and stable isotope analysis were collected from surface, 5, 10, 20, 30, 40, 50, 60 m depths. 1.5- 3 L of seawater samples were filtered through pre-combusted (500 °C for 4 hours) GF/F filters (47mm diameter; Whatman) using a vacuum pump (Tarson, Rocker 400) with pressure maintained below 200 mb. The filters were then stored inside dust-free plastic Petri-plates at -20 °C until further analysis. Before the analysis, the filters were brought to room temperature and oven-dried at 60 °C overnight. An aliquot of the filter was fumigated with HCl to remove traces of particulate inorganic carbon (if any) and again oven-dried for 4-5 hrs. The aliquots were packed in aluminum cups inside a clean bench. All accessories were cleaned with ethanol before and after packing individual samples. The samples were analyzed at ALYSES analytical platform (IRD-Sorbonne Université, Bondy, France) in an elemental analyzer (Thermo Fisher, Flash HT, USA)

coupled to an isotope ratio mass spectrophotometer (Thermo Fisher, Delta, USA). The results of $\delta^{13}\text{C}_{\text{POC}}$ were expressed in δ notation as given below against the standard (IAEA-CH-6; IAEA, Vienna, calibrated to Vienna PDB):

$$\delta^{13}\text{C}_{\text{POC}} = \left[\left\{ \frac{\left(\frac{^{13}\text{C}}{^{12}\text{C}} \right)_{\text{sample}}}{\left(\frac{^{13}\text{C}}{^{12}\text{C}} \right)_{\text{standard}}} \right\} - 1 \right] * 10^3$$

An aliquot of oven-dried filter, before acid fumigation, was taken for the N isotopic analysis. The filters were packed in aluminum cups and analyzed like $\delta^{13}\text{C}$ analysis. The results of $\delta^{15}\text{N}$ are expressed in δ notation as given below against the standard (the certified value for $\delta^{15}\text{N}$ was traceable to IAEA-N-1; IAEA, Vienna; calibrated to Air):

$$\delta^{15}\text{N}_{\text{PN}} = \left[\left\{ \frac{\left(\frac{^{15}\text{N}}{^{14}\text{N}} \right)_{\text{sample}}}{\left(\frac{^{15}\text{N}}{^{14}\text{N}} \right)_{\text{standard}}} \right\} - 1 \right] * 10^3$$

The mean uncertainties involved in $\delta^{13}\text{C}$ and $\delta^{15}\text{N}$ analyses are $\pm 0.5 \text{ ‰}$ and $\pm 0.25 \text{ ‰}$, respectively. Note that the volume of seawater filtered did not allow analytical replicates. However, based on our previous studies (for detail please see Silori et al. 2021) negligible difference was noticed between samples collected from 0 & 5 m and 50 & 60 m suggesting that these reported mean analytical uncertainties cover those related to sampling and sample processing. The minimum detection limit for C and N was $5 \mu\text{g}$ and the minimum quantity of POC and PN contents in our samples were well above this limit.

2.2 Satellite Data

The satellite data for 10 m surface winds, curl of surface 10m wind stress, and sea surface temperature (SST) was obtained from the ERDDAP server (<https://coastwatch.pfeg.noaa.gov/erddap/index.html>). Following datasets were used for 10 m surface winds, curl of surface 10m wind stress and sea surface temperature, respectively, 1) FNMOC 10m Surface Winds, 360x181, Monthly, 2) FNMOC 10m Surface Winds, 360x181, Monthly and, 3) SST, AQUA_MODIS, L3m.MO.SST.sst.4km, Masked, SMI, NASA GSFC OBPG, R2019.0, Global, 0.04166°, Science Quality, 2003-present (Monthly Composite).

2.3 Statistical Analysis

Statistical analysis was performed using Microsoft Excel 2007. Single-factor ANOVA was performed for all the parameters to calculate the statistical significance in their spatial variability. The probability

levels (p) were set to 0.05, the level of significance (p values) for different parameters are listed. Multiple correlations (at significance level $p \leq 0.05$) between various parameters were computed using PAST v4.03 (Hammer et al., 2001) software.

3. Results

3.1 Wind speeds and hydrography:

During SWM-18, substantially higher wind speeds were observed from the satellite data in the entire basin as well as along the cruise transect (64°E) (Fig. 2a). The onboard wind data showed a similar trend [SWM-18 ($9\text{--}11 \text{ m s}^{-1}$); SWM-17 ($5\text{--}10 \text{ m s}^{-1}$)]. The lowest wind speeds were observed towards the northern end of the transect, while the highest wind speeds were seen in the central region. A gradient in the wind stress curl (June-August) is also distinctly evident in the northern and southern Arabian Sea (Fig. 2b). The wind stress curl was positive north of about 19°N along 64°E during SWM-17 and SWM-18 and was well established during SWM-18 (Fig. 2b). The wind speeds also seemed to affect the extent of lateral advection of waters from the Arabian coast towards the central Arabian Sea, which is evident from the presence of cooler SSTs (Fig. 2c). During SWM-18, cooler-upwelled waters were advected further eastwards relative to SWM-17.

Consequently, there was a significant variation in the MLDs along the transect (Fig. 3). Shallower MLDs were found at the northern stations, along with the lowest wind speeds whereas deeper MLDs, consistent with the highest wind speeds, were observed towards the center of the transect. In contrast, deeper MLDs associated to moderate wind speeds were encountered towards the southern end of the transect. While the MLDs were not markedly different between the two years to the north of 16° , shallower MLDs ($60\text{--}110 \text{ m}$) were seen during SWM-17 compared to the deeper MLDs ($120\text{--}130 \text{ m}$) during SWM-18 to the south of 16°N .

The sampled stations represent a diverse set of environmental conditions, evident from the MLDs and wind speeds (Fig. 3). Hence, for further analysis, we classified the study area into three regions: i) Northern ($19^\circ\text{--}21^\circ \text{N}$); ii) Findlater Jet Axis ($16^\circ\text{--}18^\circ \text{N}$) and iii) Southern Stations ($11^\circ\text{--}15^\circ \text{N}$). The positive wind-stress curl (Fig. 2b) influenced the stations $19^\circ\text{--}21^\circ \text{N}$. During both SWM-17 and SWM-18, the shallowest MLDs co-occurred with shoaling of the 26°C isotherm at these stations in the north (Fig. 3b and 4a). Further southwards, higher wind speeds, deeper MLDs marked stations $16^\circ\text{--}18^\circ \text{N}$ and these stations seemed to be under a significant influence of the strong, low-lying southwesterly Findlater jet. Further down south, the jet's impact appeared to wear off as the wind speeds gradually decreased. These stations ($11^\circ\text{--}15^\circ \text{N}$) were marked by deeper MLDs, possibly due to the downwelling driven by the negative wind-stress curl.

The SSTs (Fig 4a, 4b) and the salinity (Fig 4c, 4d) distribution along the cruise track agreed with the seasonal evolution of surface properties. However, during SWM-18 (25.8–26.9° C), the SSTs were appreciably cooler ($p < 0.05$) than SWM-17 (26.6–27.7° C). At the northern stations, the 26°C isotherm shoaled close to ≈ 40 m (Fig. 4a, 4b). We observed the coolest SSTs at 16° N along with the highest wind speeds. The most elevated SSTs were seen at the southernmost stations, 12°N (27.8°C; SWM-17 and 26.8°C; SWM-18) and 11°N (27.7°C; SWM-17 and 26.9°C; SWM-18). Hence, the average temperature values down to 60 m were notably higher at the southern stations than the other regions.

The salinity values varied between 36.20–36.55 PSU (SWM-17) and 36.36–36.63 PSU (SWM-18) (Fig. 4c, 4d). Though the values were not remarkably different between the two cruises, a significant difference was observed in the salinity values (36.28 ± 0.10 : SWM-17 and 36.47 ± 0.12 : SWM-18) at the stations influenced by the Findlater Jet axis (Table 1). We observed low salinity values at 16°N at the surface and within the mixed layers during SWM-17 and SWM-18. The salinity values were considerably different between the three regions during SWM-17, while we observed an appreciable difference only between northern and southern stations during SWM-18. The surface DO values were not pronouncedly different between the two cruises and ranged from 5.4 mg L⁻¹ to 6.6 mg L⁻¹. Lower DO values (4 mg L⁻¹) were seen at ≈ 50 –70 m north of 16°N. Such low values were seen at or below 90 m south of 16° N. At the northern stations, the low DO waters were found closer to the surface during SWM-18 compared to SWM-17 (Fig. 4e, 4f). The Chl_a values ranged from 0.1–1.3 $\mu\text{g L}^{-1}$ during SWM-17 (Fig. 4g) and 0.05–3.1 $\mu\text{g L}^{-1}$ during SWM-18 (Fig. 4h). Higher values were observed at the surface of the northern stations and the Findlater jet axis. There was a substantial decline in the Chl_a values below 80 m. Subsurface Chlorophyll maxima were observed at Findlater Jet Axis and southern stations within 20–60m depths.

3.2 Dissolved Inorganic nutrients

The distribution of dissolved inorganic nutrients in the water column closely followed the distribution of MLDs (Fig. 5). At the northern stations, the concentrations were nearly uniform down to 40 m during SWM-17 and SWM-18 but these concentrations were remarkably higher ($p < 0.05$) during SWM-18. The vertical profile of nutrient concentrations depicts shallower nutricline at the northern stations mainly, 20 and 21°N. At the stations influenced by the Findlater jet axis, the nutrient concentrations were consistent down to 80 m and the highest amongst other regions during SWM-17. The nutricline was observed at ≈ 70 m, and the values were slightly higher during SWM-18. The nutricline gradually deepened at the stations influenced by the Findlater Jet axis, except at 16°N, where we observed an abrupt shoaling of the nutricline (Fig. 5a–5f). The extent of shoaling at 16°N seemed

more substantial during SWM-18. At southern stations, uniform nutrient concentrations were observed down to 80 m during SWM-17, while this was observed down to 120 m during SWM-18. Still, the nutrient concentrations were considerably higher for SWM-18.

In general, during SWM-17, the surface concentrations of nitrate+nitrite (Fig. 5a), DSi (Fig. 5c), and DIP (Fig. 5e) ranged between 0.1–4.9 $\mu\text{mol L}^{-1}$, 0.4–2.0 $\mu\text{mol L}^{-1}$, and 0.4–1.2 $\mu\text{mol L}^{-1}$, respectively. During SWM-18, the concentrations of nitrate+nitrite (Fig. 5b), DSi (Fig. 5d), and DIP (Fig. 5f) varied between 1.87–6.65 $\mu\text{mol L}^{-1}$, 0.16–2.48 $\mu\text{mol L}^{-1}$, and 0.2–2.2 $\mu\text{mol L}^{-1}$, respectively. Significantly higher concentrations of nitrate+nitrite and DSi ($p < 0.05$) were found during SWM-18. We measured the highest nutrient concentrations at 16° N and lowest nitrate+nitrite, and DIP concentrations at the southern stations (Table 1). The DSi concentrations were not conspicuously different amongst the three regions during SWM-17, while considerably low DSi concentrations were observed at the northern stations during SWM-18.

DSi:nitrate+nitrite (Si:N) ratios were remarkably different ($p < 0.05$) between the years (Fig. 5g, 5h); the Si:N ratios > 1 were common during SWM-17 at the northern and the southern stations, but ratios > 1 were not observed at the stations influenced by the Findlater jet axis. In contrast, Si:N ratios did not exceed 1 for most stations during SWM-18. N:P ratios were lower than the canonical N:P (16:1) Redfield ratio, though comparatively higher values were seen during SWM-18.

3.3 POC and PN variability

The concentrations of POC, PN, and their ratios are displayed in Fig. 6. Surface POC and PN concentrations varied within 6.2–19.6 $\mu\text{mol L}^{-1}$ and 1.4–2.6 $\mu\text{mol L}^{-1}$, respectively, during SWM-17 (Fig. 6a, 6c). In SWM-18, the values lay between 6.4–18.8 $\mu\text{mol L}^{-1}$ and 1.0–3.1 $\mu\text{mol L}^{-1}$ (Fig. 6b, 6d). On average, the POC and PN concentrations during SWM-17 (POC: $11.97 \pm 4 \mu\text{mol L}^{-1}$ and PN: $1.96 \pm 0.5 \mu\text{mol L}^{-1}$) were higher ($p < 0.05$) than SWM-18 (POC: $8.86 \pm 3.8 \mu\text{mol L}^{-1}$ and PN: $1.37 \pm 0.2 \mu\text{mol L}^{-1}$). During SWM-17, there was not a significant difference in POC concentrations between the northern stations ($13.08 \pm 4 \mu\text{mol L}^{-1}$) and the stations influenced by the Findlater Jet axis ($14.93 \pm 3.4 \mu\text{mol L}^{-1}$). However, the southern stations ($10.31 \pm 3.4 \mu\text{mol L}^{-1}$) had substantially lower ($p < 0.05$) concentrations (Table 1). There was a decrease in C:N ratios with depth at the northern stations, whereas the vertical variation in C:N ratios at other stations were not pronounced (Fig. 5e). Higher ratios were found at the northern stations ($6.88 \pm 2.8 \mu\text{mol L}^{-1}$) and stations influenced by the Findlater Jet ($7.31 \pm 1.6 \mu\text{mol L}^{-1}$) compared to the southern stations ($5.47 \pm 0.9 \mu\text{mol L}^{-1}$).

During SWM-18, substantially higher ($p < 0.05$) POC concentrations were seen at the northern stations ($11.7 \pm 5.6 \mu\text{mol L}^{-1}$) as compared to stations influenced by Findlater Jet ($7.6 \pm 1.8 \mu\text{mol L}^{-1}$) and the

southern stations ($7.89 \pm 2.2 \mu\text{mol L}^{-1}$). The C:N ratios (Fig. 6f) did not vary substantially within the water column down to 60 m. C:N ratios at the northern stations ($6.98 \pm 0.8 \mu\text{mol L}^{-1}$) were notably higher than the stations influenced by the Findlater Jet ($6.16 \pm 0.9 \mu\text{mol L}^{-1}$) and the southern stations ($6.26 \pm 0.8 \mu\text{mol L}^{-1}$). Despite the difference, the POC concentrations reduced significantly ($p < 0.05$) at 60 m for all the stations during both SWM-17 ($5\text{--}10 \mu\text{mol L}^{-1}$) and SWM-18 ($5\text{--}8 \mu\text{mol L}^{-1}$).

3.4 Carbon and Nitrogen Isotopic Ratios

The surface $\delta^{13}\text{C}_{\text{POC}}$ values during SWM-17 showed a considerable variation and ranged between -28.3‰ and -23.7‰ (Fig. 6g). While during SWM-18, the surface $\delta^{13}\text{C}_{\text{POC}}$ values were comparatively less varied and ranged from -25.8‰ and -23.7‰ (Fig. 6h). Overall, the $\delta^{13}\text{C}_{\text{POC}}$ values during SWM-17 ($-26.4 \pm 1.5\text{‰}$) were notably lower ($p < 0.05$) as compared to SWM-18 ($-24.5 \pm 0.6\text{‰}$). During SWM-17 and SWM-18, lower values were observed at the northern stations at deeper depths (≈ 40 and 60 m) and higher values close to the surface. The stations influenced by the Findlater Jet axis followed a similar trend with higher values close to the surface and lower values at $40\text{--}60$ m. During SWM-17, the lowest values were observed at 16°N . Amongst the southern stations at 15°N (deepest MLD), the values were less variable in the water column. Other southern stations followed a pattern similar to the northern stations, with most of the higher values at shallower depths and lower values at deeper depths. During SWM-18, the values did not show a pronounced variation within the water column. The lowest $\delta^{13}\text{C}_{\text{POC}}$ values were observed at the northern stations and the $\delta^{13}\text{C}_{\text{POC}}$ values were significantly different ($p < 0.05$) amongst the three regions (Table 1). Overall, during SWM-17, we did not find remarkable variation in the $\delta^{13}\text{C}_{\text{POC}}$ values of the three regions, except at 16°N .

The surface $\delta^{15}\text{N}_{\text{PN}}$ values ranged between 4.7 and 9.5‰ during SWM-17 (Fig. 6i) and 5.2 and 9.7‰ during SWM-18 (Fig. 6j). Overall, the $\delta^{15}\text{N}_{\text{PN}}$ values during SWM-17 ($7.03 \pm 2.84\text{‰}$) were not statistically different ($p > 0.05$) from the values from SWM-18 ($7.35 \pm 2.32\text{‰}$) but the interannual difference was notable ($p < 0.05$) amongst the stations influenced by the Findlater Jet axis ($4.94 \pm 1.7\text{‰}$: SWM-17 and $6.67 \pm 1.8\text{‰}$: SWM-18) (Table 1). During SWM-17, $\delta^{15}\text{N}_{\text{PN}}$ values at the northern stations showed considerable vertical variation. Remarkably higher values ($9.24 \pm 3\text{‰}$) were observed at the northern stations, and most of the higher values were observed at $40\text{--}60$ m depths in SWM-18. Low values of $\delta^{15}\text{N}_{\text{PN}}$ ($4.94 \pm 1.7\text{‰}$) and low variability were seen at the stations influenced by the Findlater Jet in SWM-17. The Findlater Jet stations had fewer variations in $\delta^{15}\text{N}_{\text{PN}}$ values, but the values were not low during SWM-18. In SWM-17, for the southern stations ($13\text{--}15^\circ\text{N}$), the vertical variations were minimum; the variations increased at 11° and 12°N with higher values at 60 m depth. During SWM-18, the $\delta^{15}\text{N}_{\text{PN}}$ values were uniform for the southern stations ($6.62 \pm 1.3\text{‰}$) and were comparable to the

stations influenced by the Findlater Jet ($6.66 \pm 1.9\%$). Overall, during SWM-17, $\delta^{15}\text{N}_{\text{PN}}$ values were low ($p < 0.05$) at the stations influenced by the Findlater Jet axis. The Findlater jet axis and the southern stations' values showed a linear inverse correlation with nitrate+nitrite concentrations ($R^2 = 0.50$; $n = 46$). Significantly higher values ($p < 0.05$) were observed at the northern stations, and the other two regions were comparable during SWM-18.

The correlations between POC and Chl a for the three regions during SWM-17 and SWM-18 have been displayed in Fig 7. We observed a significant positive linear correlation between POC and Chl a values at the northern stations and the Findlater Jet axis, while such trend was absent at the southern stations. The slopes for the significant correlations ranged between 3.40 and 5.99.

The correlations between different parameters for the two monsoons have been displayed in Fig. 8a and 8b. Dissolved inorganic nutrients showed a negative correlation with the temperature depicting cooler waters as the source of the nutrients. POC concentrations were well correlated to the PN and Chl a values. POC concentrations showed a negative correlation with the DSi concentration during SWM-18. $\delta^{13}\text{C}_{\text{POC}}$ values were positively correlated with temperature, salinity, POC, PN, and Si/N and negatively with the dissolved inorganic nutrients during SWM-17. During SWM-18 the $\delta^{13}\text{C}_{\text{POC}}$ values were positively correlated with the DSi concentrations and negatively correlated with $\delta^{15}\text{N}_{\text{PN}}$ values.

4. Discussion

4.1 Influence of physical forcing on the hydrography and nutrient distribution

During the SW monsoon, physical forcing like Ekman pumping (Bauer et al., 1991; Murleedharan & Prasannakumar, 1996), wind-driven mixing, and lateral advection of upwelled waters from Oman and Somalia coasts (Young & Kindle, 1994) exert a major control on the MLDs as well as nutrient distribution in the euphotic zone in the northern and central Arabian Sea (Lee et al., 2000). Weller et al. (2002) have noted the importance of wind-driven entrainment during the first half of the SW monsoon and horizontal advection dominance during the second half. With the stabilization of winds as the monsoon progresses, the nutrient input from deeper waters is likely to reduce as the wind mixing reaches a steady state (Prasannakumar et al., 2000). We sampled during the second half of the monsoon (Aug), and hence lateral advection is expected to be prominent and is discussed in the following sections. There was substantial interannual variability in the wind speeds that also affected the SSTs and nutrient distribution. Due to high spatial variability in physical forcing and its impact on biogeochemistry in the central Arabian Sea, the discussion has been organized based on the position of the Findlater Jet axis.

Northern Stations

Along with the highest wind speeds at $\approx 16^\circ$ N, the positive wind stress curl was documented north of 19° N. The satellite images for SWM-18 showed a significant eastward expansion of the coast's cooler waters (Fig. 2c), most likely driven by substantially higher wind speeds (Fig. 2a). At the northern stations, open-ocean upwelling was marked by the shallowest MLDs associated with nutrient-rich waters. Consequently, the vertical structures of temperature, dissolved inorganic nutrients, and DO shoaled towards the surface. Despite the interannual difference in the wind speeds, the MLDs at the northern stations were comparable. The higher nitrate+nitrite concentrations in the upper water column during SWM-18 could be due to the stronger upwelling. The extent of wind-driven mixing seemed to be intense as the $4 \mu\text{mol L}^{-1}$ nitrate+nitrite, and $2 \mu\text{mol L}^{-1}$ DSi isocline shoaled up to the surface during SWM-18. Earlier reports have also noted the lateral advection of nitrate-rich upwelled waters from the Omani Coast to the northern region (Young & Kindle, 1994; Kawamiya et al., 2001). The satellite SST image (Fig. 2c) for SWM-18 suggests that lateral advection could also be an important source of nutrients at these stations.

In a monsoonal system, the signature of denitrification can propagate towards the surface due to intense vertical mixing and lead to the formation of POM with substantially higher $\delta^{15}\text{N}$ values (Montoya et al., 2006). The relatively higher $\delta^{15}\text{N}_{\text{PN}}$ values (Fig. 6i,6j) reported here are comparable to the values reported by Montoya et al. (2006) from the central Arabian Sea during the intermonsoon period (May-June). Likewise, the observed $\delta^{15}\text{N}_{\text{PN}}$ values in the present study signify the importance of vertical mixing in supplying nitrate+nitrite from the denitrification zone (OMZ) to the euphotic zone. The positive correlation between nitrate+nitrite and $\delta^{15}\text{N}_{\text{PN}}$ reflected in the correlation matrix also supports this view (Fig. 8b). The northern part of the permanent OMZ in the Arabian Sea is present in this area (Banse et al. 2014) and is consistent with our observation. Similarly, high values have been noted in the Arabian Sea sediment trap samples (Gaye et al., 2005). Montoya et al. (2006) observed considerable variations in the $\delta^{15}\text{N}_{\text{PN}}$ values in the upper 200 m water column but mostly constant values below suggesting that the surface process such as phytoplankton uptake of the regenerated nitrogen play a dominant role in determining the isotopic composition of PN. To establish this connection, we have also explored the values of $\delta^{15}\text{N}_{\text{NO}_3^-}$, the chief form of inorganic nitrogen for phytoplankton consumption, from literature (Naqvi et al., 1998; Altabet et al., 1999). It reveals that the vertical profiles of $\delta^{15}\text{N}_{\text{NO}_3^-}$ show higher values (a maximum of $\sim 15\text{--}18 \text{‰}$) at about 300 m in the OMZ in the northeastern Arabian Sea than its western and central part (the maximum is $\sim 12 \text{‰}$). In the instance of the total consumption of NO_3^- the $\delta^{15}\text{N}$ of the PN produced would converge closer to the

$\delta^{15}\text{N}_{\text{NO}_3^-}$ of the source NO_3^- (Sigman & Casciotti, 2001), otherwise, the biomass produced is depleted in ^{15}N relative to the initial nitrogen source (Montoya & McCarthy, 1995). Such high values were also noticed along with low nitrate+nitrite concentrations close to the surface at the northern stations during SWM-17. This could signify a near complete removal of nitrate+nitrite from the surface layer by phytoplankton, resulting in the production of POM with higher $\delta^{15}\text{N}_{\text{PN}}$ values. During SWM-18, the $\delta^{15}\text{N}_{\text{PN}}$ values were mostly uniform, indicating greater vertical mixing, except the higher values observed below the MLDs at the northern stations, which were most likely the result of shallower MLDs and the presence of deep waters carrying high $\delta^{15}\text{N}_{\text{PN}}$ signature.

As a consequence of upwelling supplying nutrients, the highest POC contents were measured in the northern stations, particularly at 20°- 21° N. The significant positive correlation between POC and Chla concentration (Fig. 7a, b) suggests its autochthonous origin and the influence of terrestrial particles can be overruled as already reported by Huang et al. (2018). A similar trend is also reflected in the correlation matrix (Fig. 8). Lower concentrations of DSi and $\text{Si:N} < 0.3$ indicate the removal of DSi and a possible DSi limitation which is likely due to the dominance of larger diatoms (Tarran et al., 1998) at the northern stations particularly during SWM-18. Moreover, as the sampling was done during the second half of SWM, the signature of upwelling can be shadowed by strong nutrient uptake coupled with high phytoplankton biomass (Fig. 8). Morrison et al. (1998) reported Si:N ratios of ≈ 0.5 in the waters upwelling to the surface along the coast of Oman and Somalia and suggested a potential DSi limitation in these waters. Young and Kindle (1994) utilized the silicate tracer model to show a significant decline in the advected waters' DSi concentrations. DSi limitation was also reported in the surface waters along the coast of Oman and Somalia, where significant upwelling occurs and pointed to the switch from weak DSi limitation to a strong DSi and DIN limitations towards the open ocean (Kone et al., 2006). The advected nitrate-rich waters from the Oman coast during SWM-18 seemed to alleviate the nitrogen limitation, but low DSi concentrations may limit diatom-induced POC production in this region. However, the "non-diatom" phytoplankton may consume this available nitrogen to contribute to the POC pool. During SWM-17, nitrate+nitrite concentrations $< 1 \mu\text{mol L}^{-1}$, $\text{Si:N} > 1$ and $\text{N:P} \approx 1$ indicated nitrogen limitation in the northern region. During SWM-17, the upwelled waters from the coastal regions did not seem to influence the northern stations. Similarly, low N:P values have been noted by Mantoura et al. (1993) and Malcolm et al. (1999). The C:N ratios were close to the Redfield ratio of 6.63 and were comparable to the previous reports ($\sim < 6.6$) from the Arabian Sea (Martiny et al., 2013). However, low nitrate+nitrite concentrations at 21° N could drive the distinctly high C:N ratios during SWM-17. Studies have shown that under nutrient limitation, phytoplankton accumulate carbon reserves (Griffiths & Harrison, 2009; Rodolfi et al., 2009).

The axis of the Findlater Jet and Southern Stations.

High wind speeds have been observed previously at around 16.5° N along 64° E and were attributed to the Findlater Jet axis's (Findlater, 1969) presence (Prasannakumar et al., 2001). Consistently, the maximum wind speeds between 16 -18° N were also recorded during SWM-17 and 18. Consequently, the stations between 16-18° N were marked by deeper MLDs, coolest temperatures, and higher concentrations of nutrients. During SWM-17, higher nutrient concentrations were observed at the stations influenced by the Findlater Jet axis, particularly 16° N denoting the importance of wind-driven mixing and lateral advection at these stations. The surface circulation is directly driven by wind, and an eastward flow of surface currents was noticed from the Somali and Oman coast towards the central Arabian Sea (Beal et al. 2013). The nitrate+nitrite concentrations observed during SWM-17 were comparable to the concentrations ($\approx 4 \mu\text{mol L}^{-1}$) reported by Souza et al. (1996). Additionally, slightly lower salinity values in this region (Fig. 3) could also be attributed to waters from the Somali upwelling region (Prasannakumar et al., 2000). This signal was possibly diminished in 2018 due to high wind speed-driven evaporation, which is also supported by the temperature drop along the axis of the Findlater jet.

Notably, lower $\delta^{15}\text{N}_{\text{PN}}$ values during SWM-17 at the stations influenced by the axis also hints at the presence of the laterally advected nitrogen. The values of $\delta^{15}\text{N}_{\text{PN}}$ in the surface waters can be lower when phytoplankton consume the regenerated nitrogen from the subsurface waters where denitrification is absent. Accordingly, the global average deep-water $\delta^{15}\text{N}_{\text{NO}_3^-}$ values in the absence of denitrification is lower ($5\pm 0.6\text{‰}$; Sigman et al., 1997). Due to the absence of denitrification in the western and northwestern Arabian Sea, the $\delta^{15}\text{N}_{\text{NO}_3^-}$ values of the upwelled nitrate that is further laterally advected are expected to be lower than the values generated within the OMZ. In SWM-17, due to moderate to low wind speed, the contribution of wind-driven vertical mixing in supplying nitrogen to the Findlater Jet axis was probably lesser than lateral advection. Therefore, there is no denitrification signature in $\delta^{15}\text{N}_{\text{PN}}$. Conversely, during SWM-18, both the wind-driven vertical mixing and lateral advection could be significant due to high speed. Hence, slightly higher $\delta^{15}\text{N}_{\text{PN}}$ values ($\approx 6.6\text{‰}$) were most likely due to the upward propagation of the isotopic signature of denitrification through intense vertical mixing, which was stronger than SWM-17.

At the southern stations, we observed deeper MLDs and moderate wind speeds that gradually decreased on moving southwards. Negative wind stress curl in this region is known to drive the downward Ekman pumping that progresses to deepen the mixed layers (Bauer et al., 1992; Gardener et al., 1999). The gradual shoaling of MLDs on moving equatorward during SWM-17 resulted from

reduced wind speeds and higher SSTs that enhanced thermal stratification and diminished vertical mixing compared to SWM-18. Higher wind speeds during SWM-18 seemed to control the dissolved inorganic nutrient availability in the mixed layers by affecting the extent of lateral advection (Prasannakumar et al., 2000). McCreary et al. (1996) and Kawamiya et al. (2001) also suggested eastward advection of nitrate enriched waters off the coast of Somalia to the central Arabian Sea. In SWM-18, the moderate $\delta^{15}\text{N}_{\text{PN}}$ values (6.62 ± 1.34 ‰), lie in between $\delta^{15}\text{N}_{\text{PN}}$ values derived from average deep waters and waters influenced by denitrification. Hence, this suggests the contribution of both lateral advection and vertical mixing in supplying nitrogen to the surface. Conversely, during SWM-17, the downward pumping negatively impacted the nutrient availability and the lateral advection of nutrient-rich waters from Somalia too seems negligible at the southern stations. Thus the high $\delta^{15}\text{N}_{\text{PN}}$ values noted at the southern stations (7.48 ± 2.96 ‰) during SWM-17 indicate that the regenerated nitrogen is mostly added from the denitrification zone to the surface.

In general, there was a pronounced inter-annual variation in the POC and PN concentrations for the stations influenced by the Findlater Jet axis and the stations south of it. The effect of variable wind speeds was evident on the MLDs at the southern stations. The changes in MLDs coincided with POC and PN distributions. Despite the interannual variability in nutrient levels, the POC and PN concentrations were higher during SWM-17. The significant positive correlation between POC and *Chl a* along the axis of the Findlater jet indicates an autotrophic in situ origin (Fig. 7c and d). The weakening of SW monsoon winds is usually followed by the detrainment of the nutrients in the euphotic zones (McCreary et al., 1996). During SWM-17, the wind speeds reached a peak in July, and relaxation in speeds was observed thereafter, complemented by the substantially shallower MLDs compared to SWM-18. Similarly, Gundersen et al. (1998) observed the shoaling of MLD and increased POC concentrations followed the substantial decrease in wind speeds during the late SW monsoon in 1995.

In SWM-18, the deepest MLDs (≈ 120 m) and low POC and PN concentrations were found south of the jet's axis. The mixed layer deepening during SWM-18 may have exceeded the critical compensation depth (<1% sunlight penetration), which does not allow significant *Chl a* and POC development due to light limitation. Arnone et al. (1998) noted a 20-30% reduction in the photosynthetically available radiation at the sea-surface during SW monsoon associated with the cloud cover. Gardener et al. (1999) reported a 1 % light level at about 50-65 m in the central Arabian Sea during the SW monsoon. Deepening of MLD may dilute the phytoplankton accumulation near the surface by homogenizing the constituents throughout the mixed layer and prevent a full-fledged phytoplankton bloom (Gardener et al., 1999). The correlation between *Chl a* and POC was lost south

to the Findlater Jet axis pointing towards a different source of POC rather than autochthonous. McCreary et al (1996) showed in a model-based study that particles from the Somali upwelling can be advected towards the central Arabian Sea and in that case, a decoupling between POC and Chl a can be expected. Moreover, the dominance of the microbial loop in the central Arabian Sea has also been noticed in the earlier study, particularly under oligotrophic conditions and the advected dissolved organic carbon from the Somali upwelling may support the microbial loop in the central Arabian Sea (Blackford and Burkill, 2002).

Inter-annual variability in POC

Based on the prevailing atmospheric forcing and nutrient enrichment in the euphotic zone, a higher POC was expected in 2018 than in 2017 which contrasts with our observations. The timing of the onset of SW monsoon is likely to be responsible for such interannual variability. The development of offshore phytoplankton bloom (Fig. 9) can lag behind the coastal upwelling by up to a month (Brock & McClain, 1992). Hence, the delayed monsoon onset during 2018 (Athira et al., 2020) presumably delayed the open-ocean phytoplankton biomass development. Higher nutrient, along with lower POC concentrations particularly, at the stations influenced by the Findlater Jet axis and south of it during SWM-18, indicate early uptake stage. Whereas comparatively lower nutrient concentrations, higher POC contents during SWM-17 point to an advanced phytoplankton bloom development stage. To check this, a simple mass balance calculation was done based on the available nitrate+nitrite levels above the nutricline for all stations. According to the Redfield ratio, 16 μmol of nitrogen could support 106 μmol of POC if other nutrients are not limiting. If we consider that DSi limitation may eventually hinder diatom growth, other non-diatom phytoplankton may occupy the niche and potentially contribute to POC development. Likewise, the uptake of average nitrate+nitrite concentrations ($1.64 \pm 1.5 \mu\text{mol L}^{-1}$) in SWM-17 could double the POC from the observed value ($12.3 \pm 3.4 \mu\text{mol L}^{-1}$). Whereas the remaining nitrate+nitrite ($4.16 \pm 1.70 \mu\text{mol L}^{-1}$) in SWM-18 could increase the observed POC value by four times ($36.6 \pm 12.6 \mu\text{mol L}^{-1}$). We have tried to interlink the POM dynamics during SWM-17 and 18 with the phytoplankton and zooplankton abundance (Supplementary Table 1). It was noticed that zooplankton biomass was more than five times higher in SWM-17 than in SWM-18 (Chowdhury et al. under review). Conversely, phytoplankton cell densities showed a reverse trend. The abundance and life-cycles of zooplankton are often closely tied to a prior increase in phytoplankton biomass (Mahara et al., 2019). This suggests the relative contribution of zooplankton to POC was higher during SWM-17 indicating that a major part of phytoplankton was already transferred to the secondary trophic level. Whereas in SWM-18, the phytoplankton abundance was yet to reach its peak. The slope of the linear equation between POC and Chl a in the north for SWM-18

was lower than the value noticed in SWM-17 suggesting there was more Chl_a relative to POC signifying an early growth phase (Fig. 7a, 7b); a similar trend was also noted in the axis of the Findlater Jet (Fig. 7c and 7d).

4.2 Variability in $\delta^{13}\text{C}_{\text{POC}}$

Marine phytoplankton exhibit $\delta^{13}\text{C}_{\text{POC}}$ values within the range of -19.9 to -24.8‰ (Bauer et al., 2002), mostly due to the fractionation of inorganic carbon during the process of photosynthesis (Goericke and Fry, 1994). Most of the values we observed during SWM-18 within the upper water column fall within the lower values of this range (-24 to -25‰, Fig. 6h). However, the values of $\delta^{13}\text{C}_{\text{POC}}$ during SWM-17 were slightly but significantly lower (-25 to -27 ‰, Figure 6g). A possible contribution of partially remineralized organic matter from the OMZ to the surface water may also interfere with the in situ produced phytoplankton biomass and result in much lower values of $\delta^{13}\text{C}_{\text{POC}}$. However, this possibility can be overruled due to the significant linear correlation between POC and Chl_a contents with a slope value similar to the open ocean region (Huang et al. 2018) particularly for the northern stations and Findlater Jet axis. The carbon isotopic composition data is comparatively sparse from the Arabian Sea. The average $\delta^{13}\text{C}_{\text{POC}}$ values ($\approx -25.5 \pm 1.4$ ‰) noticed in the present study were well within the range of values reported from the Arabian Sea (-26.3 and -23.5 ‰; Krishna et al., 2018) and Bay of Bengal (-26.3 and -24.1 ‰; Sherin et al. 2018).

The trends in $\delta^{13}\text{C}_{\text{POC}}$ values could also be directed by the composition and the size structure of the phytoplankton community (Rau et al., 1990; Esposito et al., 2019). We have also reported that changing phytoplankton community directly influences the $\delta^{13}\text{C}_{\text{POC}}$ values in the eastern Arabian Sea during SWM-17 (Silori et al. 2021). In general, diatoms are the major constituents of the microphytoplankton community and are relatively enriched in ^{13}C (Goering et al., 1990; Harmelin-Vivien et al., 2008) while in several studies (Rau et al., 1990; Loick et al., 2007), lower $\delta^{13}\text{C}_{\text{POC}}$ values have been ascribed to the picophytoplankton and nanophytoplankton. The dominance of large diatoms was noticed in the north and axis of the Findlater Jet and smaller phytoplankton in the south (Chowdhury et al, under review). However $\delta^{13}\text{C}_{\text{POC}}$ values did not co-vary with the changing phytoplankton community structure indicating the influence of other factors.

The observed interannual variability in $\delta^{13}\text{C}_{\text{POC}}$ values can be attributed to the phytoplankton bloom development phase. As has been mentioned earlier in section 4.1, an early growth phase with fast-growing phytoplankton can produce high $\delta^{13}\text{C}_{\text{POC}}$ values as has been noticed in SWM-18. We have noticed in our previous study in the coastal Arabian Sea during the SWM-17 (Silori et al. 2021) that the fast-growing phytoplankton under nutrient replete conditions fractionate less and produce high

$\delta^{13}\text{C}_{\text{POC}}$ values (Burkhardt et al., 1999; Riebesell et al. 2000). On the contrary, in SWM-17 significantly lower values of $\delta^{13}\text{C}_{\text{POC}}$ can be due to 1) matured growth phase; 2) higher contribution of zooplankton. A greater zooplankton abundance during SWM-17 may contribute to the significantly lower $\delta^{13}\text{C}_{\text{POC}}$ values. Indeed, though there might be a minor ($<1\text{‰}$) ^{13}C enrichment in zooplankton relative to their diet (Grey et al., 2001), the zooplankton fecal pellets can be highly depleted in ^{13}C as opposed to their diet (Tamelander et al., 2006). Accordingly, the slightly higher $\delta^{15}\text{N}_{\text{PN}}$ values at the southern stations were during SWM-17 can be attributed to enhanced zooplankton abundance. The highest values of $\delta^{15}\text{N}_{\text{PN}}$ within the euphotic zone of the northern stations (Fig. 6i) could be attributed to highest zooplankton abundance. The presence of low oxygenated water below this zone may force them to accumulate in that area. Consumers are often enriched in ^{15}N relative to their food (DeNiro & Epstein, 1981; Wada et al., 1987). The isotopic fractionation is negligible during the assimilation and ingestion (Altabet & Small, 1990) but the process of production and excretion of NH_4^+ as the primary waste product discriminates against ^{15}N , increasing the $\delta^{15}\text{N}$ within the consumer's tissues (Bada et al., 1989). This recycling loop is reasonably effective and does not allow the NH_4^+ to accumulate in the mixed layers by complete nitrification (Montoya, 2008). The uptake of relatively depleted $^{15}\text{NH}_4^+$ by phytoplankton after nitrification could mask the higher $\delta^{15}\text{N}_{\text{PN}}$ values usually reported for zooplankton and could be the reason for insignificant interannual differences.

Lower $\delta^{13}\text{C}_{\text{POC}}$ values at the base of the euphotic zone were noted by earlier studies (Trull & Armand, 2001; Close & Henderson, 2020) and ascribed to the dominance of smaller average cell size of phytoplankton. Some compound-specific isotope analyses of lipids have supported a photosynthetic origin of low $\delta^{13}\text{C}_{\text{POC}}$ values in the lower euphotic zone (Eadie & Jeffrey, 1973). Isotopic composition of POC is also affected by the degradation of ^{13}C enriched labile POC constituents leading to the accumulation of ^{13}C depleted lipids (Eadie & Jeffrey, 1973). However we did not observe a simultaneous increase in C:N ratio with depth that could have been indicative of increasing lipid concentrations. A few different mechanisms could potentially drive lower values observed at deeper depths. Saino (1992) suggested higher CO_2 concentrations in the lower euphotic zone, and growth rates restricted by light limitation could lead to lower $\delta^{13}\text{C}_{\text{POC}}$ values (Close & Henderson, 2020). Likewise, we have shown in our earlier studies that lower values of $\delta^{13}\text{C}_{\text{POC}}$ at the base of the euphotic zone can be attributed to light limitation as well as heterotrophic dominance (Biswas et al. 2017; Silori et al. 2021).

4.3 The implication for POC export flux

Earlier studies reported that the SW monsoon with moderate wind speed was associated with the highest particle flux dominated by biogenic opal (Rixen et al., 2005). Moreover, the dominance of large diatoms like *Rhizosolenia* was noticed in the sediment trap samples. These features suggest that higher DSi enrichment along with other nutrients driven by strong upwelling is the key force to initiate such large diatom bloom followed by rapid sinking. The large size of diatoms cells also helps in escaping from zooplankton grazing and is expected to sink rapidly due to higher ballasting. Gauns et al. (2005) showed that the relative contribution of phytoplankton, zooplankton, and bacteria to POC changes seasonally depending on the physicochemical variability. The authors also observed that the export flux potential of POC was maximum during the SW monsoon when the relative contribution of phytoplankton was the highest. Based on this information we hypothesize (Fig. 9) the following process

Stronger upwelling → higher nutrient input with more DSi → larger diatoms → less grazing rate → rapid sinking and higher POC export flux

Weaker upwelling → less nutrient input with less DSi → smaller diatoms/non-diatom → high grazing rate → slow and lower POC export flux

The inter-annual variability in ocean-atmosphere coupling driven by monsoon onset and wind speeds, among other factors, controls the carbon export flux in the Arabian Sea (Rixen et al. 2019). Higher wind speeds strengthen the coastal and open-ocean upwelling intensities, resulting in increased primary productivity and, therefore, enhanced carbon fluxes (Haake et al., 1993; Rixen et al., 2019). During SWM-18, the higher nutrient concentrations are expected to result in larger phytoplankton cells (diatoms) that are not only effective in escaping grazers (Hansen et al., 1997) but sink efficiently. Chowdhury et al. (under review) noted the abundance of larger diatoms such as *Rhizosolenia* in SWM-18 (Supplementary Table 1). While during SWM-17, the limited lateral advection and wind-driven mixing suggest the presence of smaller phytoplankton cells that can be effectively grazed by zooplankton. Grazing affects the efficiency of the carbon export, as it allows the fragmentation of phytoplankton aggregates, and the fecal pellets thus produced are remineralized faster in the upper water column (Dagg et al., 2014). The effective transfer of the carbon produced to a higher trophic level and linking of the classical food web to the microbial loop lowers the carbon flux (Pasternak et al., 2009). Hence, apart from the wind-driven primary productivity, the relative contribution of phytoplankton and zooplankton to the POC pool might also affect the carbon fluxes in the Arabian

Sea. This fact is likely to impact the organic carbon export flux to the mesopelagic and control the distribution and intensification of the OMZ in the Arabian Sea.

Conclusions:

- The impact of interannual variability in SW monsoon wind was evident on most of the measured parameters
- Open ocean upwelling was recorded towards the northern side with shallow MLDs where high POC contents were noticed; whereas towards the Findlater Jet Axis, the highest wind speeds prevailed with relatively lower POC contents
- The correlation between POC and Chl a concentrations at northern stations and the axis of the Findlater Jet reveals that the main source of POC was phytoplankton; whereas the insignificant correlation points towards heterotrophic dominance in the southern stations
- With changing phytoplankton bloom phase and the relative contribution of phytoplankton and zooplankton to the total POC pool, the $\delta^{13}\text{C}_{\text{POC}}$ values exhibited substantial interannual variability
- $\delta^{15}\text{N}_{\text{PN}}$ signature suggested the supply of nitrogen from the denitrification zone (OMZ) via vertical mixing in the northern stations; whilst, the signature of lateral advection from the Somali /Oman upwelling was reflected in the axis of the Findlater Jet.
- $\delta^{15}\text{N}_{\text{PN}}$ values indicate that in SWM-17, due to lower wind speeds lateral advection might have dominated over vertical mixing in the Findlater jet axis; whereas during SWM-18, due to high wind speed both processes contributed to nitrogen input to the euphotic zone
- Any future change in the atmospheric forcing, particularly in wind speed and SST, thus may potentially alter wind stress curl, upwelling intensity, nutrient input as well as carbon export flux in this area

Acknowledgment

This study was supported by CSIR funding (MLP 1802). The help and support extended by the Director, CSIR NIO is acknowledged. We express our sincere thanks to the captain, scientists, technical staff, ship cell staff, crew members, deckhand, and the students onboard RV Sindhu Sadhana (SSD 040; SSD 55). We also acknowledge UGC, DST, and CSIR for funding the first, second, and third authors, respectively. We also acknowledge IRD. (France) for funding and carrying out the isotopic analyses. Original data can be accessed by contacting the corresponding author. NIO contribution number is XXXX (will be provided after the acceptance). We have no conflict of interest to declare.

References

1. Altabet, M. A., Murray, D. W., & Prell, W. L. (1999). Climatically linked oscillations in Arabian Sea denitrification over the past 1 m.y.: Implications for the marine N cycle. *Paleoceanography*, 14(6), 732–743. <https://doi.org/10.1029/1999PA900035>
2. Altabet, M. A., & Small, L. F. (1990). Nitrogen isotopic ratios in fecal pellets produced by marine Zooplankton. *Geochimica et Cosmochimica Acta*, 54(1), 155–163. [https://doi.org/10.1016/0016-7037\(90\)90203-W](https://doi.org/10.1016/0016-7037(90)90203-W)
3. Arnone, R. A., Ladner, S., La Violette, P. E., Brock, J. C., & Rochford, P. A. (1998). Seasonal and interannual variability of surface photosynthetically available radiation in the Arabian Sea. *Journal of Geophysical Research: Oceans*, 103(3334), 7735–7748. <https://doi.org/10.1029/97jc03204>
4. Athira, U. N., Abhilash, S., & sathiyamoorthy, V. (2020). Distinct atmosphere-ocean coupling processes on the onset phase of Indian summer monsoon during 2017 and 2018 as revealed through SCATSAT-1 and its comparison with CFSv2. *International Journal of Remote Sensing*, 41(20), 8014–8033. <https://doi.org/10.1080/01431161.2020.1767827>
5. Bada, J. L., Schoeninger, M. J., & Schimmelmann, A. (1989). Isotopic fractionation during peptide bond hydrolysis. *Geochimica et Cosmochimica Acta*, 53(12), 3337–3341. [https://doi.org/10.1016/0016-7037\(89\)90114-2](https://doi.org/10.1016/0016-7037(89)90114-2)
6. Banse, K. (1987). Seasonality of phytoplankton chlorophyll in the central and northern Arabian sea. *Deep Sea Research Part A, Oceanographic Research Papers*, 34(5–6), 713–723. [https://doi.org/10.1016/0198-0149\(87\)90032-X](https://doi.org/10.1016/0198-0149(87)90032-X)
7. Banse, K., Naqvi, S. W. A., Narvekar, P. V., Postel, J. R., & Jayakumar, D. A. (2014). Oxygen minimum zone of the open Arabian Sea: variability of oxygen and nitrite from daily to decadal timescales. *Biogeosciences*, 11(8), 2237–2261. <https://doi.org/10.5194/bg-11-2237-2014>
8. Bauer, S., Hitchcock, G. L., & Olson, D. B. (1991). Influence of monsoonally-forced Ekman dynamics upon surface layer depth and plankton biomass distribution in the Arabian Sea. *Deep Sea Research Part A, Oceanographic Research Papers*, 38(5), 531–553. [https://doi.org/10.1016/0198-0149\(91\)90062-K](https://doi.org/10.1016/0198-0149(91)90062-K)
9. Beal, L. M., Hormann, V., Lumpkin, R., & Foltz, G. R. (2013). The response of the surface circulation of the Arabian Sea to monsoonal forcing. *Journal of Physical Oceanography*, 43(9), 2008–2022.
10. Bhosle, N. B., Dhople, V. M., & Wagh, A. B. (1988). Distribution of particulate organic carbon in the central Arabian Sea. *Proc. Indian Acad. Sci. (Earth Planet. Sci.) (Vol. 97)*.
11. Blackford, J. C., & Burkill, P. H. (2002). Planktonic community structure and carbon cycling in the Arabian Sea as a result of monsoonal forcing: the application of a generic model. *Journal of Marine Systems*, 36(3–4), 239–267.
12. Brandes, J. A., & Devol, A. H. (2002). A global marine-fixed nitrogen isotopic budget: Implications for Holocene nitrogen cycling. *Global Biogeochemical Cycles*, 16(4), 67–1–67–14. <https://doi.org/10.1029/2001gb001856>
13. Brock, J. C., & McClain, C. R. (1992). Interannual variability in phytoplankton blooms observed in the northwestern Arabian Sea during the south-west monsoon. *Journal of Geophysical Research*, 97(C1), 733–750. <https://doi.org/10.1029/91JC02225>
14. Buesseler, K., Ball, L., Andrews, J., Benitez-Nelson, C., Belostock, R., Chai, F., & Chao, Y. (1998). Upper ocean export of particulate organic carbon in the Arabian Sea derived from thorium-234. *Deep-Sea Research Part II: Topical Studies in Oceanography*, 45(10–11), 2461–2487. [https://doi.org/10.1016/S0967-0645\(98\)80022-2](https://doi.org/10.1016/S0967-0645(98)80022-2)
15. Burkhardt, S., Riebesell, U., & Zondervan, I. (1999). Stable carbon isotope fractionation by marine phytoplankton in response to daylength, growth rate, and CO₂ availability. *Marine Ecology Progress Series*, 184, 31–41.

16. Burkill, P. H., Mantoura, R. F. C., & Owens, N. J. P. (1993). Biogeochemical cycling in the northwestern Indian Ocean: a brief overview. *Deep-Sea Research Part II*, 40(3), 643–649. [https://doi.org/10.1016/0967-0645\(93\)90049-S](https://doi.org/10.1016/0967-0645(93)90049-S)
17. Close, H. G., & Henderson, L. C. (2020). Open-ocean minima in $\delta^{13}\text{C}$ values of particulate organic carbon in the lower euphotic zone. *Frontiers in Marine Science*. <https://doi.org/10.3389/fmars.2020.540165>
18. Dagg, M. J., Jackson, G. A., & Checkley, D. M. (2014). The distribution and vertical flux of fecal pellets from large zooplankton in Monterey bay and coastal California. *Deep-Sea Research Part I: Oceanographic Research Papers*, 94, 72–86. <https://doi.org/10.1016/j.dsr.2014.09.001>
19. Deniro, M. J., & Epstein, S. (1981). Influence of diet on the distribution of nitrogen isotopes in animals. *Geochimica et Cosmochimica Acta*, 45(3), 341–351. [https://doi.org/10.1016/0016-7037\(81\)90244-1](https://doi.org/10.1016/0016-7037(81)90244-1)
20. Eadie, B. J., & Jeffrey, L. M. (1973). $\delta^{13}\text{C}$ analyses of oceanic particulate organic matter. *Marine Chemistry*, 1(3), 199–209. [https://doi.org/10.1016/0304-4203\(73\)90004-2](https://doi.org/10.1016/0304-4203(73)90004-2)
21. Esposito, M., Achterberg, E. P., Bach, L. T., Connelly, D. P., Riebesell, U., & Taucher, J. (2019). Application of Stable Carbon Isotopes in a Subtropical North Atlantic Mesocosm Study: A New Approach to Assess CO₂ Effects on the Marine Carbon Cycle. *Frontiers in Marine Science*, 6(October), 1–17. <https://doi.org/10.3389/fmars.2019.00616>
22. Findlater, J. (1977). Observational aspects of the low-level cross-equatorial jet stream of the western Indian Ocean. *Pure and Applied Geophysics PAGEOPH*, 115(5–6), 1251–1262. <https://doi.org/10.1007/BF00874408>
23. Gardner, W. D., Gundersen, J. S., Richardson, M. J., & Walsh, I. D. (1999). The role of seasonal and diel changes in mixed-layer depth on carbon and chlorophyll distributions in the Arabian Sea. *Deep-Sea Research Part II: Topical Studies in Oceanography*, 46(8–9), 1833–1858. [https://doi.org/10.1016/S0967-0645\(99\)00046-6](https://doi.org/10.1016/S0967-0645(99)00046-6)
24. Gauns, M., Madhupratap, M., Ramaiah, N., Jyothibabu, R., Fernandes, V., Paul, J. T., & Prasanna Kumar, S. (2005). Comparative accounts of biological productivity characteristics and estimates of carbon fluxes in the Arabian Sea and the Bay of Bengal. In *Deep-Sea Research Part II: Topical Studies in Oceanography* (Vol. 52, pp. 2003–2017). <https://doi.org/10.1016/j.dsr2.2005.05.009>
25. Gaye-Haake, B., Lahajnar, N., Emeis, K. C., Unger, D., Rixen, T., Suthhof, A., et al. (2005). Stable nitrogen isotopic ratios of sinking particles and sediments from the northern Indian Ocean. *Marine Chemistry*, 96(3–4), 243–255. <https://doi.org/10.1016/j.marchem.2005.02.001>
26. Goericke, R., & Fry, B. (1994). Variation of marine plankton $\delta^{13}\text{C}$ with latitude, temperature and dissolved CO₂ in world ocean, 8(1), 85–90.
27. Goering, J., Alexander, V., & Haubenstein, N. (1990). Seasonal variability of stable carbon and nitrogen isotope ratios of organisms in a North Pacific Bay. *Estuarine, Coastal and Shelf Science*, 30(3), 239–260. [https://doi.org/10.1016/0272-7714\(90\)90050-2](https://doi.org/10.1016/0272-7714(90)90050-2)
28. Grasshoff, K., Kremling, K., & Ehrhardt, M. (1992). *Methods of Seawater Analysis*. John Wiley & Sons, Ltd.
29. Grey, J., Jones, R. I., & Sleep, D. (2001). Seasonal changes in the importance of the source of organic matter to the diet of zooplankton in Loch Ness, as indicated by stable isotope analysis. *Limnology and Oceanography*, 46(3), 505–513. <https://doi.org/10.4319/lo.2001.46.3.0505>
30. Griffiths, M. J., & Harrison, S. T. L. (2009). Lipid productivity as a key characteristic for choosing algal species for biodiesel production. *Journal of Applied Phycology*, 21(5), 493–507. <https://doi.org/10.1007/s10811-008-9392-7>
31. Gundersen, J. S., Gardner, W. D., Richardson, M. J., & Walsh, I. D. (1998). Effects of monsoons on the seasonal and spatial distributions of POC and chlorophyll in the Arabian Sea. *Deep-Sea Research Part II: Topical Studies in Oceanography*, 45(10–11), 2103–2132. [https://doi.org/10.1016/S0967-0645\(98\)00065-4](https://doi.org/10.1016/S0967-0645(98)00065-4) Gupta, G. V. M., Sudheesh, V., Sudharma, K. V., Saravanane, N., Dhanya, V., Dhanya, K. R., et al. (2016). Evolution to decay of upwelling and

- associated biogeochemistry over the southeastern Arabian Sea shelf. *Journal of Geophysical Research: Biogeosciences*, 121(1), 159–175. <https://doi.org/10.1002/2015JG003163>
32. Haake, B., Ittekkot, V., Ramaswamy, V., Nair, R. R., & Honjo, S. (1992). Fluxes of amino acids and hexosamines to the deep Arabian Sea. *Marine Chemistry*, 40(3-4), 291-314.
 33. Haake, B., Ittekkot, V., Rixen, T., Ramaswamy, V., Nair, R. R., & Curry, W. B. (1993). Seasonality and interannual variability of particle fluxes to the deep Arabian sea. *Deep-Sea Research Part I*, 40(7), 1323–1344. [https://doi.org/10.1016/0967-0637\(93\)90114-I](https://doi.org/10.1016/0967-0637(93)90114-I)
 34. Hammer, D. A. T., Ryan, P. D., Hammer, Ø., & Harper, D. A. T. (2001). Past: Paleontological Statistics Software Package for Education and Data Analysis. *Palaeontologia Electronica* (Vol. 4). Retrieved from http://palaeo-electronica.orghttp://palaeo-electronica.org/2001_1/past/issue1_01.htm.
 35. Hansen, P. J., Bjørnson, P. K., & Hansen, B. W. (1997). Zooplankton grazing and growth: Scaling within the 2-2,-µm body size range. *Limnology and Oceanography*, 42(4), 687–704. <https://doi.org/10.4319/lo.1997.42.4.0687>
 36. Harmelin-Vivien, M., Loizeau, V., Mellon, C., Beker, B., Arlhac, D., Bodiguel, X., et al. (2008). Comparison of C and N stable isotope ratios between surface particulate organic matter and microphytoplankton in the Gulf of Lions (NW Mediterranean). *Continental Shelf Research*, 28(15), 1911–1919. <https://doi.org/10.1016/j.csr.2008.03.002>
 37. Kawamiya, M. (2001). Mechanism of offshore nutrient supply in the Western Arabian Sea. *Journal of Marine Research*, 59(5), 675–696. <https://doi.org/10.1357/002224001762674890>
 38. Kharbush, J. J., Close, H. G., Van Mooy, B. A. S., Arnosti, C., Smittenberg, R. H., Le Moigne, F. A. C., et al. (2020, June 26). Particulate Organic Carbon Deconstructed: Molecular and Chemical Composition of Particulate Organic Carbon in the Ocean. *Frontiers in Marine Science*. Frontiers Media SA <https://doi.org/10.3389/fmars.2020.00518>
 39. Koné, V., Aumont, O., Lévy, M., & Resplandy, L. (2009). Physical and biogeochemical controls of the phytoplankton seasonal cycle in the Indian Ocean: A modeling study. In *Geophysical Monograph Series* (Vol. 185, pp. 147–166). American Geophysical Union. <https://doi.org/10.1029/2008GM000700>
 40. Le Moigne, F. A. C. (2019). Pathways of Organic Carbon Downward Transport by the Oceanic Biological Carbon Pump. *Frontiers in Marine Science*, 6, 634. <https://doi.org/10.3389/fmars.2019.00634>
 41. Lee, C. M., Jones, B. H., Brink, K. H., & Fischer, A. S. (2000). The upper-ocean response to monsoonal forcing in the Arabian Sea: Seasonal and spatial variability. *Deep-Sea Research Part II: Topical Studies in Oceanography*, 47(7–8), 1177–1226. [https://doi.org/10.1016/S0967-0645\(99\)00141-1](https://doi.org/10.1016/S0967-0645(99)00141-1)
 42. Lee, C., Murray, D. W., Barber, R. T., Buesseler, K. O., Dymond, J., Hedges, J. I., et al. (1998). Particulate organic carbon fluxes: compilation of results from the 1995 US JGOFS Arabian Sea Process Study: By the Arabian Sea Carbon Flux Group. *Deep Sea Research Part II: Topical Studies in Oceanography*, 45(10–11), 2489–2501. [https://doi.org/10.1016/S0967-0645\(98\)00079-4](https://doi.org/10.1016/S0967-0645(98)00079-4)
 43. Loick, N., Dippner, J., Doan, H. N., Liskow, I., & Voss, M. (2007). Pelagic nitrogen dynamics in the Vietnamese upwelling area according to stable nitrogen and carbon isotope data. *Deep-Sea Research Part I: Oceanographic Research Papers*, 54(4), 596–607. <https://doi.org/10.1016/j.dsr.2006.12.009>
 44. Mahara, N., Pakhomov, E. A., Jackson, J. M., & Hunt, B. P. (2019). Seasonal zooplankton development in a temperate semi-enclosed basin: Two years with different spring bloom timing. *Journal of Plankton Research*, 41(3), 309–328. <https://doi.org/10.1093/plankt/fbz016>
 45. Malcolm, E., Woodward, S., Rees, A. P., & Stephens, J. A. (1999). The influence of the south-west monsoon upon the nutrient biogeochemistry of the Arabian Sea. *Deep-Sea Research Part II: Topical Studies in Oceanography*, 46(3–4), 571–591. [https://doi.org/10.1016/S0967-0645\(98\)00118-0](https://doi.org/10.1016/S0967-0645(98)00118-0)

46. Mantoura, C., Law, C. S., J.P. Owens, N., Burkill, P. H., Malcolm, E., J.M. Howland, R., & Llewellyn, C. A. (1993). Nitrogen biogeochemical cycling in the northwestern Indian Ocean. *Deep-Sea Research Part II*, 40(3), 651–671. [https://doi.org/10.1016/0967-0645\(93\)90050-W](https://doi.org/10.1016/0967-0645(93)90050-W)
47. Martiny, A. C., Vrugt, J. A., Primeau, F. W., & Lomas, M. W. (2013). Regional variation in the particulate organic carbon to nitrogen ratio in the surface ocean. *Global Biogeochemical Cycles*, 27(3), 723–731. <https://doi.org/10.1002/gbc.20061>
48. McCreary, J. P., Kohler, K. E., Hood, R. R., & Olson, D. B. (1996). A four-component ecosystem model of biological activity in the Arabian Sea. *Progress in Oceanography*, 37, 193–240. [https://doi.org/S0079-6611\(96\)00005-5](https://doi.org/S0079-6611(96)00005-5)
49. Montoya, J. P. (2008). Nitrogen Stable Isotopes in Marine Environments. *Nitrogen in the Marine Environment*, (September), 1277–1302. <https://doi.org/10.1016/B978-0-12-372522-6.00029-3>
50. Montoya, J. P., & McCarthy, J. J. (1995). Isotopic fractionation during nitrate uptake by phytoplankton grown in continuous culture. *Journal of Plankton Research*, 17(3), 439–464. <https://doi.org/10.1093/plankt/17.3.439>
51. Montoya, J. P., Voss, M., & Sea, B. (2006). Nitrogen Cycling in Suboxic Waters : Isotopic Signatures of Nitrogen Transformation in the Arabian Sea Oxygen Minimum Zone. In Neretin LN (Ed.), *Past and present Water column Anoxia* (pp. 259–281). Springer. <https://doi.org/10.1007/1-4020-4297-3>
52. Morrison, J. ., Codispoti, L. ., Gaurin, S., Jones, B., Manghnani, V., & Zheng, Z. (1998). Seasonal variation of hydrographic and nutrient fields during the US JGOFS Arabian Sea Process Study. *Deep Sea Research Part II: Topical Studies in Oceanography*, 45(10–11), 2053–2101. [https://doi.org/10.1016/S0967-0645\(98\)00063-0](https://doi.org/10.1016/S0967-0645(98)00063-0)
53. Muraleedharan, P. M., & PrasannaKumar, S. (1996). Arabian Sea upwelling - A comparison between coastal and open ocean regions. *Current Science*, 71(11), 842–846.
54. Nair, R. R., Ittekkot, V., Manganini, S. J., Ramaswamy, V., Haake, B., Degens, E. T., et al. (1989). Increased particle flux to the deep ocean related to monsoons. *Nature*, 338(6218), 749–751. <https://doi.org/10.1038/338749a0>
55. Naqvi, S. W. A. (1994). Denitrification processes in the Arabian Sea. *Proceedings of the Indian Academy of Sciences - Earth and Planetary Sciences*, 103(2), 279–300. <https://doi.org/10.1007/BF02839539>
56. Naqvi, S. W. A., Naik, H., Pratihary, A., D'Souza, W., Narvekar, P. V., Jayakumar, D. A., et al. (2006). Coastal versus open-ocean denitrification in the Arabian Sea. *Biogeosciences*, 3(4), 621–633. <https://doi.org/10.5194/bg-3-621-2006>
57. Naqvi, S. W. A., Noronha, R. J., Somasundar, K., & Sen Gupta, R. (1990). Seasonal changes in the denitrification regime of the Arabian Sea. *Deep Sea Research Part A, Oceanographic Research Papers*, 37(4), 593–611. [https://doi.org/10.1016/0198-0149\(90\)90092-A](https://doi.org/10.1016/0198-0149(90)90092-A)
58. Naqvi, S. W. A., Yoshinari, T., Jayakumar, D. A., Altabet, M. A., Narvekar, P. V., Devol, A. H., et al. (1998). Budgetary and biogeochemical implications of N₂O isotope signatures in the Arabian Sea. *Nature*, 394(6692), 462–464. <https://doi.org/10.1038/28828>
59. Pasternak, A., Hagen, W., Kattner, G., Michels, J., Graeve, M., & Schnack-Schiel, S. B. (2009). Lipid dynamics and feeding of dominant Antarctic calanoid copepods in the eastern Weddell Sea in December. *Polar Biology*, 32(11), 1597–1606. <https://doi.org/10.1007/s00300-009-0658-6>
60. Prasanna Kumar, S., Madhupratap, M., Dileep Kumar, M., Gauns, M., Muraleedharan, P. M., Sarma, V. V. S. S., & De Souza, S. N. (2000). Physical control of primary productivity on a seasonal scale in central and eastern Arabian Sea. *Proceedings of the Indian Academy of Sciences, Earth and Planetary Sciences*, 109(4), 433–441. <https://doi.org/10.1007/bf02708331>
61. Ramaiah, N., Raghukumar, S., & Gauns, M. (1996). Bacterial abundance and production in the central and eastern Arabian Sea. *Current Science*, 71(11), 878–882.
62. Rau, G. H., Takahashi, T., Des Marais, D. J., Repeta, D. J., & Martin, J. H. (1992). The relationship between $\delta^{13}\text{C}$ of organic matter and $[\text{CO}_2(\text{aq})]$ in ocean surface water: Data from a JGOFS site in

- the northeast Atlantic Ocean and a model. *Geochimica et Cosmochimica Acta*, 56(3), 1413–1419. [https://doi.org/10.1016/0016-7037\(92\)90073-R](https://doi.org/10.1016/0016-7037(92)90073-R)
63. Riebesell, U., Burkhardt, S., Dauelsberg, A., & Kroon, B. (2000). Carbon isotope fractionation by a marine diatom: dependence on the growth-rate-limiting resource.
 64. Rixen, T., Cowie, G., Gaye, B., Goes, J., Do, H., Gomes, R., et al. (2020). Reviews and syntheses: Present, past, and future of the oxygen minimum zone in the northern Indian Ocean. *Biogeosciences*, 17, 6051–6080. <https://doi.org/10.5194/bg-17-6051-2020>
 65. Rixen, T., Gaye, B., & Emeis, K. C. (2019, July 1). The monsoon, carbon fluxes, and the organic carbon pump in the northern Indian Ocean. *Progress in Oceanography*. Elsevier Ltd. <https://doi.org/10.1016/j.pocean.2019.03.001>
 66. Rixen, T., Guptha, M. V. S., & Ittekkot, V. (2005). Deep ocean fluxes and their link to surface ocean processes and the biological pump. *Progress in Oceanography*, 65(2-4 SPEC. ISS.), 240–259. <https://doi.org/10.1016/j.pocean.2005.03.006>
 67. Rixen, T., Haake, B., Ittekkot, V., & Nair, R. R. (1996). Coupling between SW monsoon-related surface and deep ocean processes as discerned from continuous particle flux measurements and correlated satellite data. *Progress in Oceanography*, 101(C12), 569–582. Retrieved from <http://doi.wiley.com/10.1029/96JC02420>
 68. Rodolfi, L., Zittelli, G. C., Bassi, N., Padovani, G., Biondi, N., Bonini, G., & Tredici, M. R. (2009). Microalgae for oil: Strain selection, induction of lipid synthesis and outdoor mass cultivation in a low-cost photobioreactor. *Biotechnology and Bioengineering*, 102(1), 100–112. <https://doi.org/10.1002/bit.22033>
 69. Sarkar, A., Naqvi, S. W. A., Lavik, G., Pratihary, A., Naik, H., Shirodkar, G., & Kuypers, M. M. M. (2020). Massive Nitrogen Loss Over the Western Indian Continental Shelf During Seasonal Anoxia: Evidence From Isotope Pairing Technique. *Frontiers in Marine Science*, 7, 678. <https://doi.org/10.3389/fmars.2020.00678>
 70. Sarma V. V. S. S., Dileep Kumar, M., MD, G., & Rajendran, A. (1996). Seasonal variations in inorganic carbon components in the central and eastern Arabian Sea. *Current Science*, 71(11), 852–856.
 71. Sarma, V. V. S. S., Bhaskar, T. U., Kumar, J. P., & Chakraborty, K. (2020). Potential mechanisms responsible for occurrence of core oxygen minimum zone in the north-eastern Arabian Sea. *Deep Sea Research Part I: Oceanographic Research Papers*, 165, 103393.
 72. Sherin, C. K., Sarma, V. V. S. S., Rao, G. D., Viswanadham, R., Omand, M. M., & Murty, V. S. N. (2018). New to total primary production ratio (f-ratio) in the Bay of Bengal using isotopic composition of suspended particulate organic carbon and nitrogen. *Deep Sea Research Part I: Oceanographic Research Papers*, 139, 43–54.
 73. Shetye, S. S., Kurian, S., Vidya, P. J., Gauns, M., Shenoy, D. M., Aparna, S. G., et al. (2021). Total organic carbon and its role in oxygen utilization in the eastern Arabian Sea. *Marine Pollution Bulletin*, 163, 111939. <https://doi.org/10.1016/j.marpolbul.2020.111939>
 74. Sigman, D. M., & Casciotti, K. L. (2001). Nitrogen isotopes in the ocean, (1997), 1884–1894. <https://doi.org/10.1006/rwos.2001.0172>
 75. Silori, S., Sharma, D., Chowdhury, M., Biswas, H., Bandyopadhyay, D., Shaik, A. U. R., ... & Narvekar, J. (2021). Contrasting phytoplankton and biogeochemical functioning in the eastern Arabian Sea shelf waters recorded by carbon isotopes. *Marine Chemistry*, 103962.
 76. Smith, R. L., & Bottero, J. (1977). On upwelling in the Arabian Sea. Pergamon Press New York.
 77. Smith, S. L., Banse, K., Cochran, J. K., Codispoti, L. A., Ducklow, H. W., Luther, M. E., et al. (1991). US JGOFS: Arabian Sea Process Study US JGOFS Planning Report, No. 13. Massachusetts.
 78. Subha Anand, S., Rengarajan, R., & Sarma, V. V. S. S. (2018). ²³⁴Th-Based Carbon Export Flux Along the Indian GEOTRACES GI02 Section in the Arabian Sea and the Indian Ocean. *Global Biogeochemical Cycles*, 32(3), 417–436. <https://doi.org/10.1002/2017GB005847>

79. Tamelander, T., Sørenseide, J. E., Hop, H., & Carroll, M. L. (2006). Fractionation of stable isotopes in the Arctic marine copepod *Calanus glacialis*: Effects on the isotopic composition of marine particulate organic matter. *Journal of Experimental Marine Biology and Ecology*, 333(2), 231–240. <https://doi.org/10.1016/j.jembe.2006.01.001>
80. Tarran, G. A., Burkill, P. H., Edwards, E. S., & Woodward, E. M. S. (1999). Phytoplankton community structure in the Arabian Sea during and after the SW monsoon, 1994. *Deep-Sea Research Part II: Topical Studies in Oceanography*, 46(3–4), 655–676. [https://doi.org/10.1016/S0967-0645\(98\)00122-2](https://doi.org/10.1016/S0967-0645(98)00122-2)
81. Trull, T. W., & Armand, L. (2001). Insights into Southern Ocean carbon export from the $\delta^{13}\text{C}$ of particles and dissolved inorganic carbon during the SOIREE iron release experiment. *Deep-Sea Research Part II: Topical Studies in Oceanography*, 48(11–12), 2655–2680. [https://doi.org/10.1016/S0967-0645\(01\)00013-3](https://doi.org/10.1016/S0967-0645(01)00013-3)
82. UNESCO, 1994. Protocols for the Joint Global Ocean Flux Study (JGOFS), Core Measurements, IOC Manuals and Guides 29. UNESCO, Paris, p. 170.
83. Voss, M., Dippner, J. W., & Montoya, J. P. (2001). Nitrogen isotope patterns in the oxygen-deficient waters of the Eastern Tropical North Pacific Ocean. *Deep-Sea Research Part I: Oceanographic Research Papers*, 48(8), 1905–1921. [https://doi.org/10.1016/S0967-0637\(00\)00110-2](https://doi.org/10.1016/S0967-0637(00)00110-2)
84. Wada, E. (1987). ^{15}N and ^{13}C Abundances in Marine Environments with Emphasis on Biogeochemical Structure of Food Web. *Isotopenpraxis Isotopes in Environmental and Health Studies*, 23(9), 320–322. <https://doi.org/10.1080/10256018708623831>
85. Winkler, L. W. (1888). Die Bestimmung des im Wassergelösten Sauerstoffes. *Berichte Der Deutschen Chemischen Gesellschaft*, 21(2), 2843–2854. <https://doi.org/10.1002/cber.188802102122>
86. Young, D. K., & Kindle, J. C. (1994). Physical processes affecting availability of dissolved silicate for diatom production in the Arabian Sea. *Journal of Geophysical Research*, 99(C11), 22619. <https://doi.org/10.1029/94jc01449>

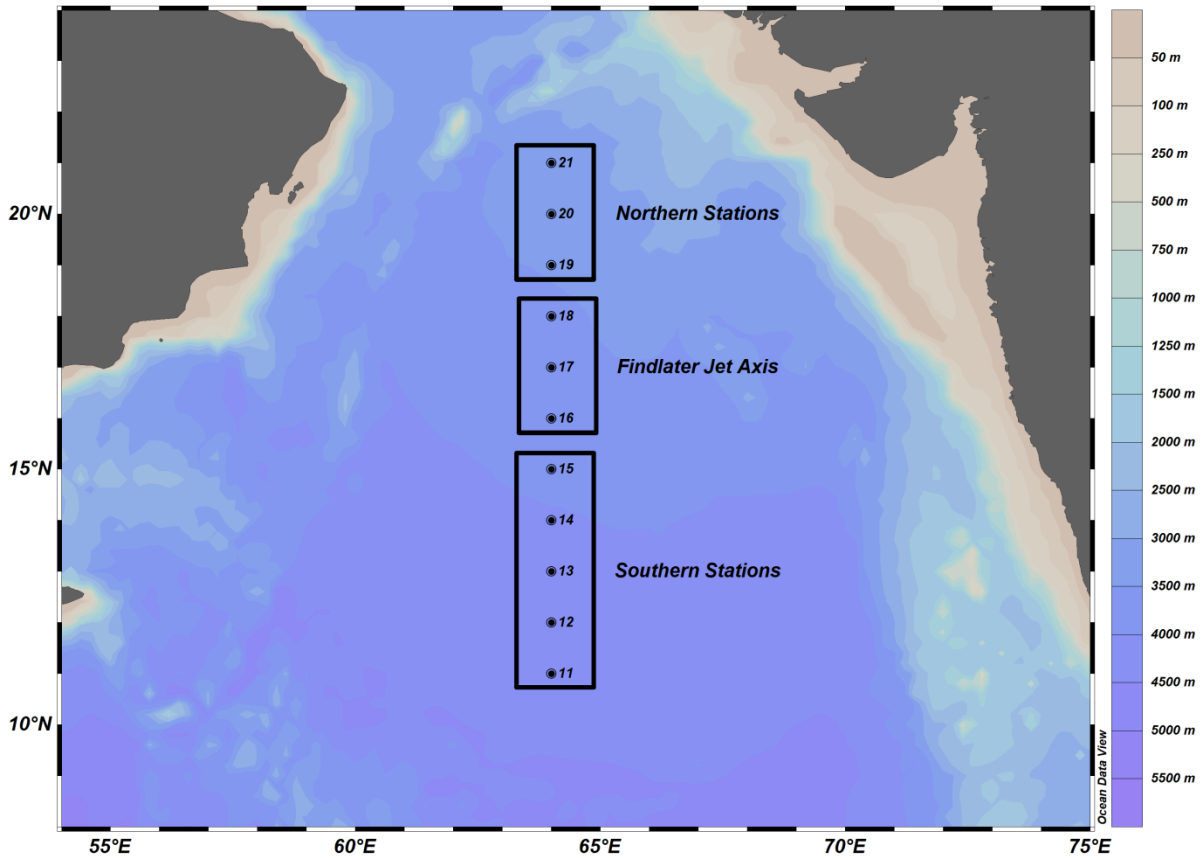


Figure 1: Map showing the cruise track and the station locations. A total of 11 stations were sampled at one-degree intervals. The stations were classified into three regions: i) Northern (19°–21°N); ii) Findlater Jet Axis (16°–18°N) and iii) Southern Stations (11°–15°N) depending on the distinct physical processes dominant in the region.

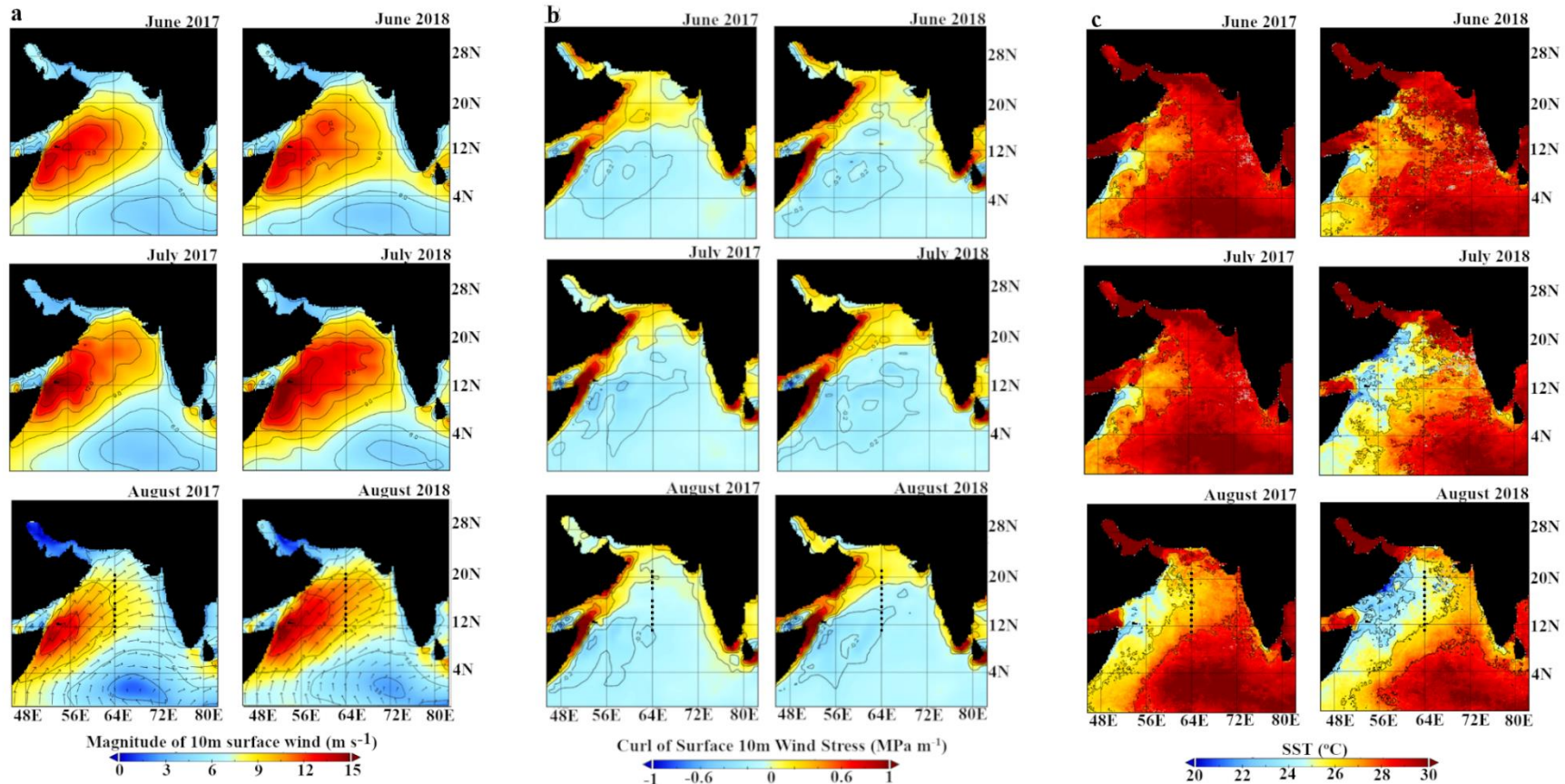


Figure 2: Monthly mean **a)** 10 m surface wind speed (m s^{-1}); **b)** Curl of surface 10m wind stress ($10^{-8} \text{ Pa m}^{-1}$); **c)** Sea Surface Temperature (SST) ($^{\circ}\text{C}$) for June -August during 2017 and 2018. The last panel of each figure displays the sampling locations. The data set was obtained from the ERDDAP server; for wind speed and wind stress curl FNMOC 10m Surface Winds, 60x181 was used; for SST the following data set has been used: AQUA_MODIS, L3m.MO.SST.sst.4km, Masked, SMI, NASA GSFC OBPB, R2019.0, Global, 0.04166 $^{\circ}$, Science Quality, 2003-present.

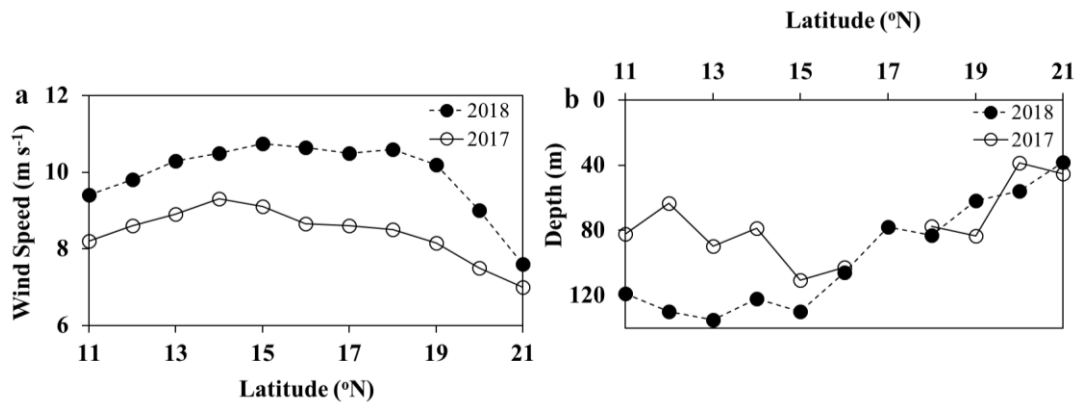


Figure 3: **a)** The recorded wind speeds onboard; **b)** Mixed Layer Depths (MLDs) for each station. The wind speeds were significantly higher in 2018 than in 2017.

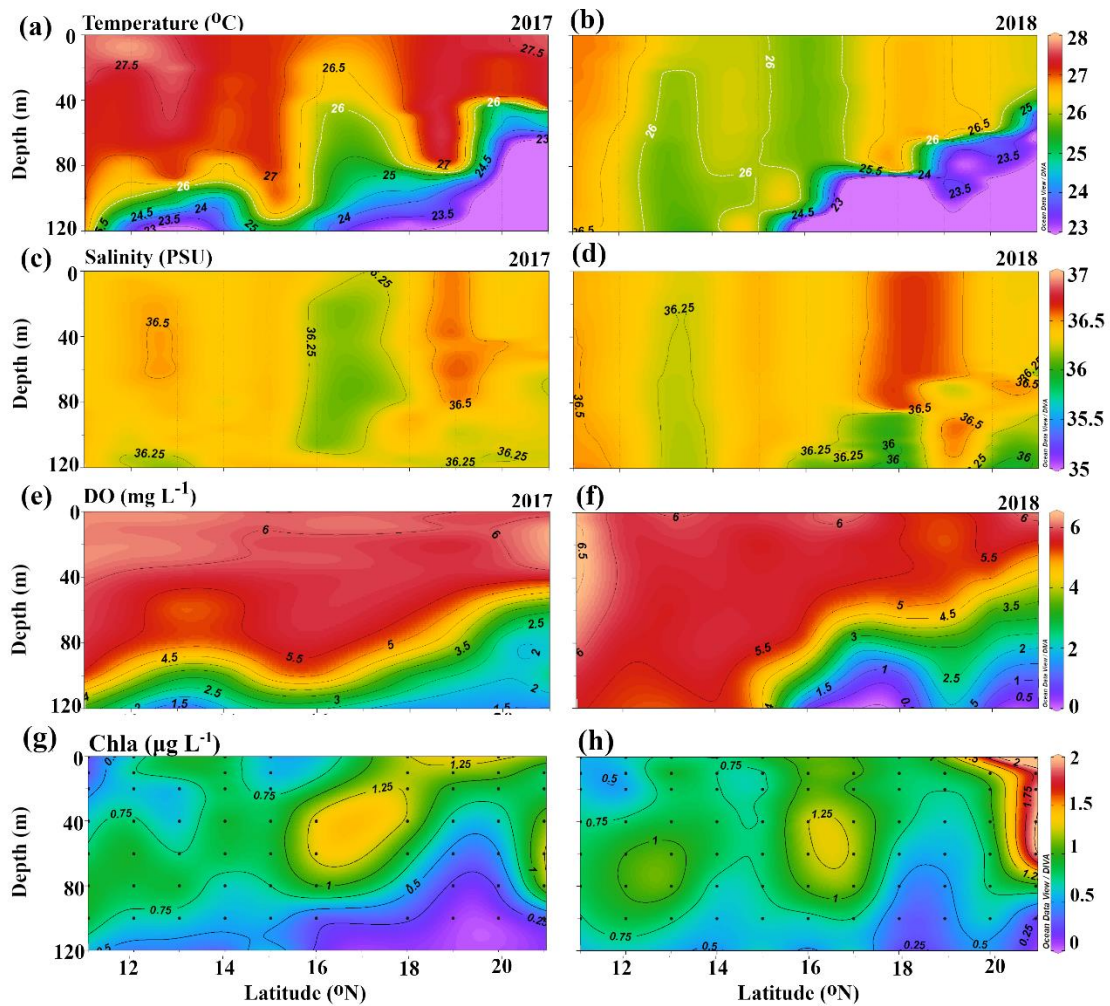


Figure 4: The vertical profiles of water temperature during **a**) 2017; **b**) 2018 (white isotherm depict 26°C; the vertical profiles of salinity during **c**) 2017; **d**) 2018; the distribution of dissolved oxygen (DO) **e**) 2017 and **f**) 2018; vertical profiles of fluorescence (Chla) detected from the CTD sensor during **g**) 2017 and **h**) 2018 along the cruise track down to 120 m. Temperature, salinity and DO profiles have been plotted down to 120 m to depict the hydrography of the entire mixed layer depth, though the POC, PN, and isotopes were sampled till 60 m depth.

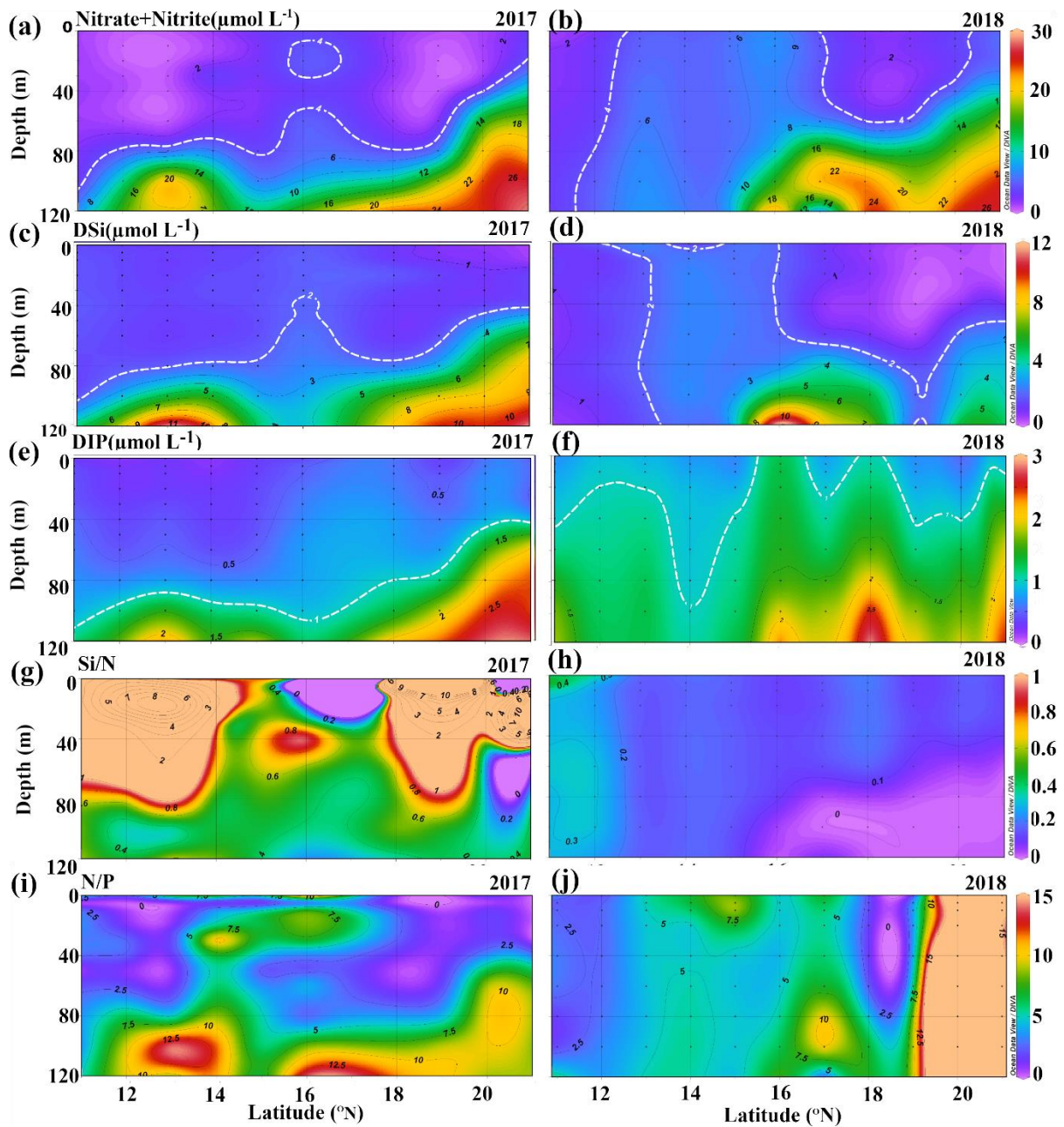


Figure 5: Vertical profiles of nitrate+nitrate (DIN) ($\mu\text{mol L}^{-1}$) during **a)** 2017;**b)**2018 (white isoline depicts $4\mu\text{mol L}^{-1}$); DSi ($\mu\text{mol L}^{-1}$) during **c)** 2017; **d)** 2018 (white isoline depicts $2\mu\text{mol L}^{-1}$); DIP ($\mu\text{mol L}^{-1}$) during **e)** 2017; **f)** 2018 (white isoline depicts $1\mu\text{mol L}^{-1}$) and the ratios of DSi: DIN during **g)** 2017; **h)** 2018; the ratios between DIN:DIP **i)** 2017, and **j)** 2018 down to 120 m. The concentrations of dissolved inorganic nutrients have been plotted down to 120 m to highlight the contrast between above and below the mixed layer.

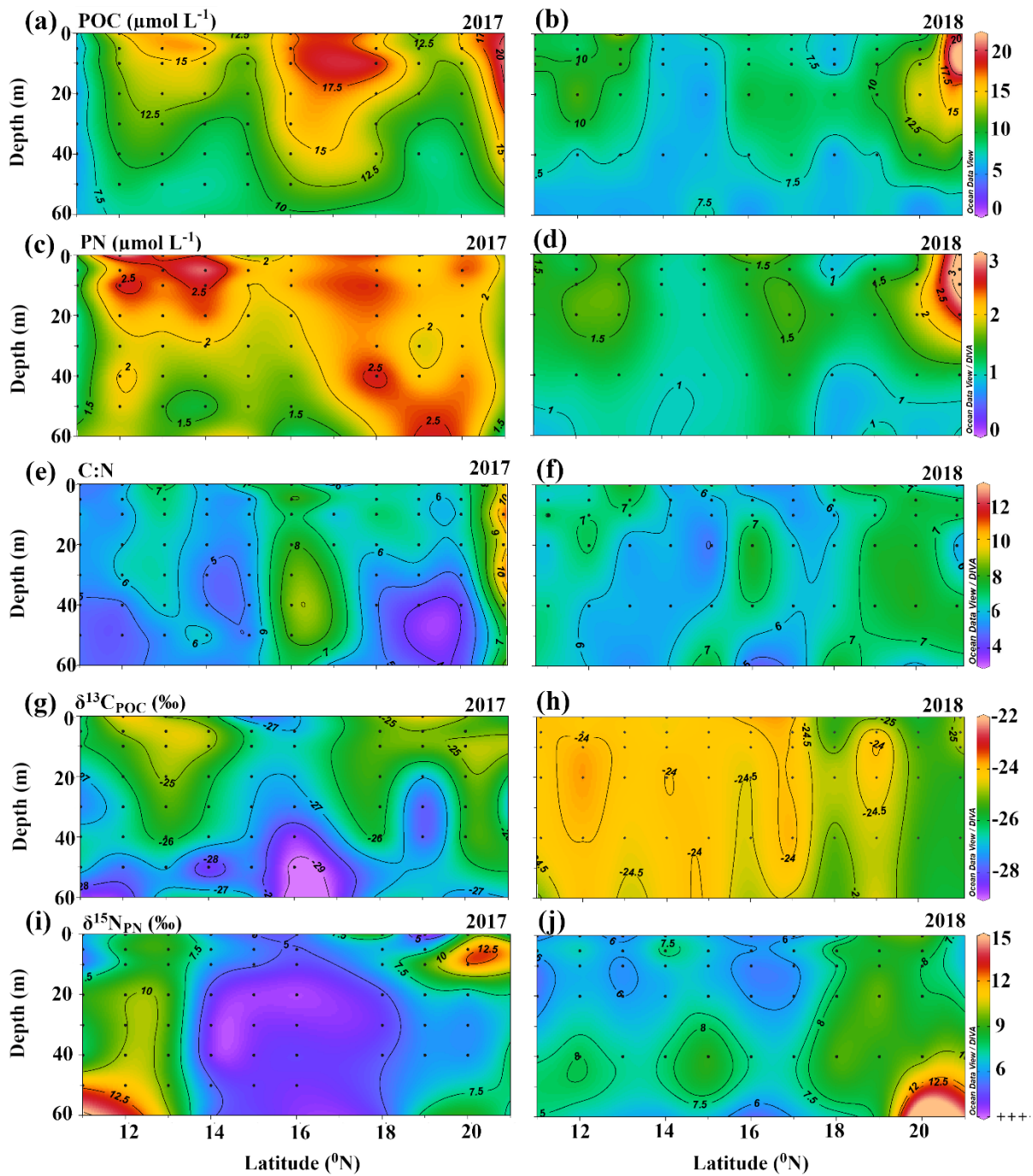


Figure 6: Vertical profiles of POC ($\mu\text{mol L}^{-1}$) during **a**) 2017; **b**) 2018; PN ($\mu\text{mol L}^{-1}$) during **c**) 2017; **d**) 2018; C:N ratio during **e**) 2017; **f**) 2018; $\delta^{13}\text{C}_{\text{POC}}(\text{‰})$ during **g**) 2017;**h**) 2018 and $\delta^{15}\text{N}_{\text{PN}}(\text{‰})$ during **i**) 2017; **j**) 2018 down to 60 m depth.

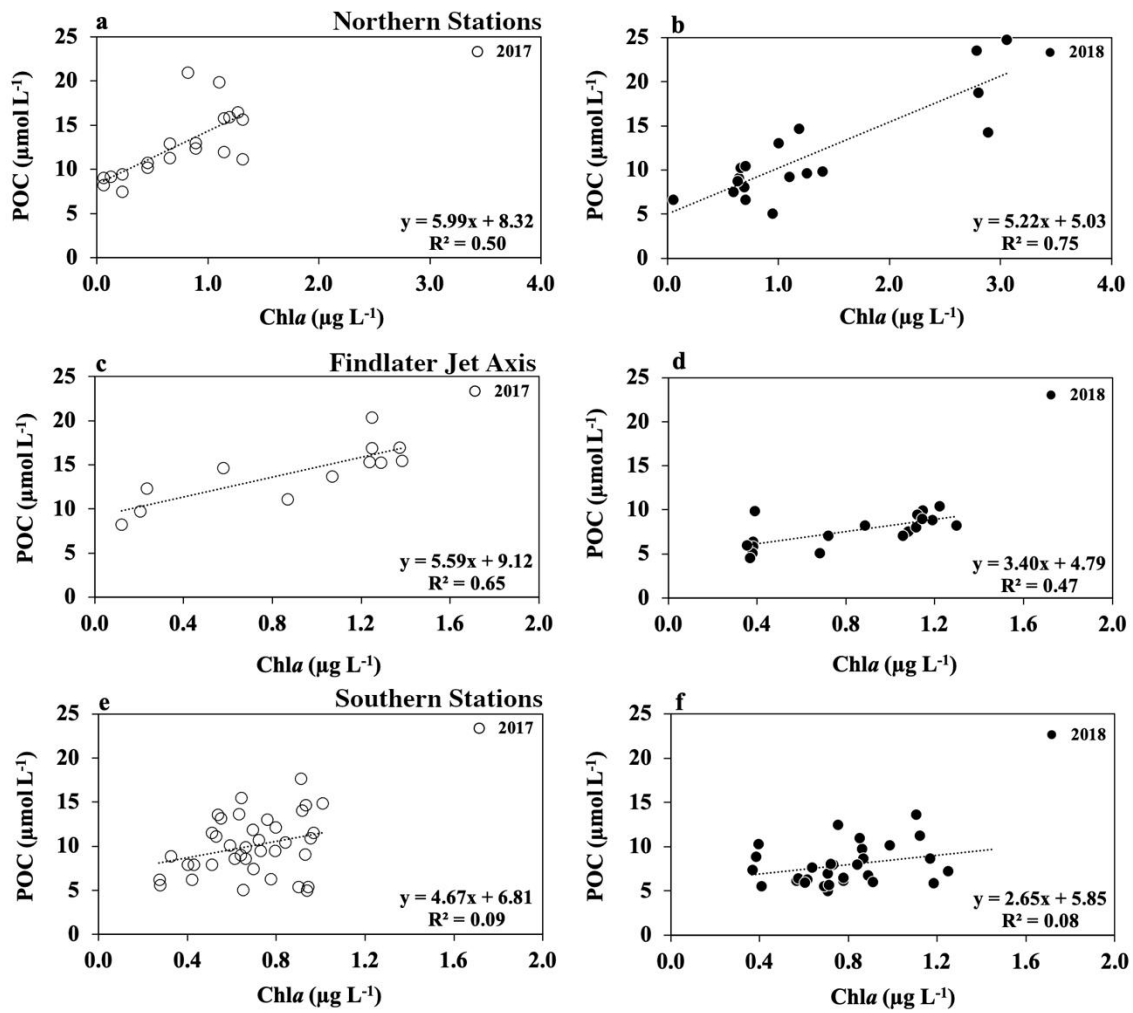


Figure 7: The correlation between POC and Chla at the northern stations during **a)** 2017; **b)** 2018; the correlation between POC and Chla at the Findlater jet axis during **c)** 2017; **d)** 2018; the correlation between POC and Chla at the southern stations during **e)** 2017; **f)** 2018.

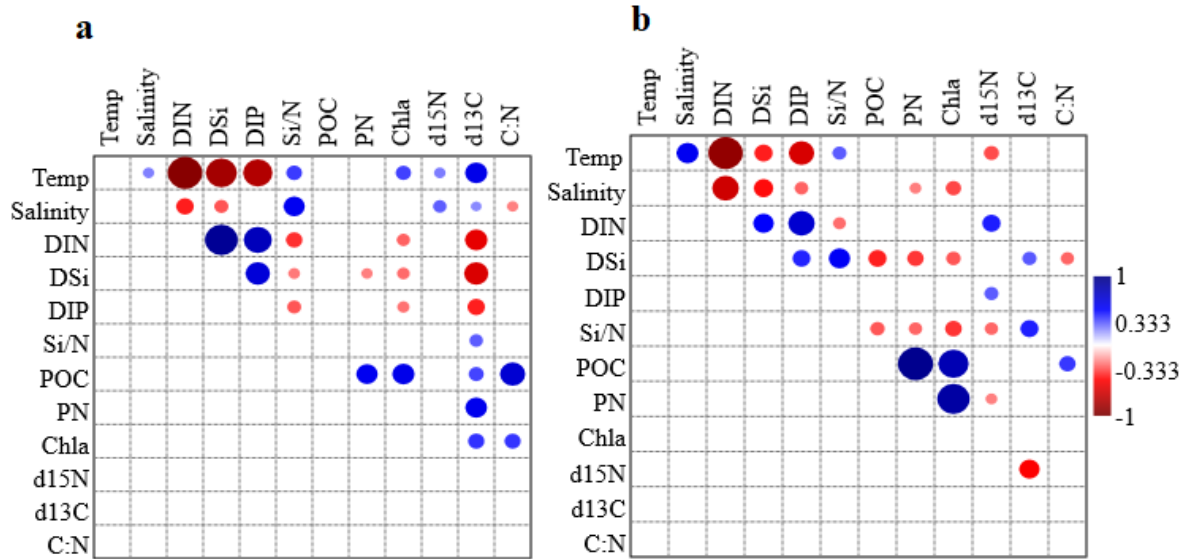
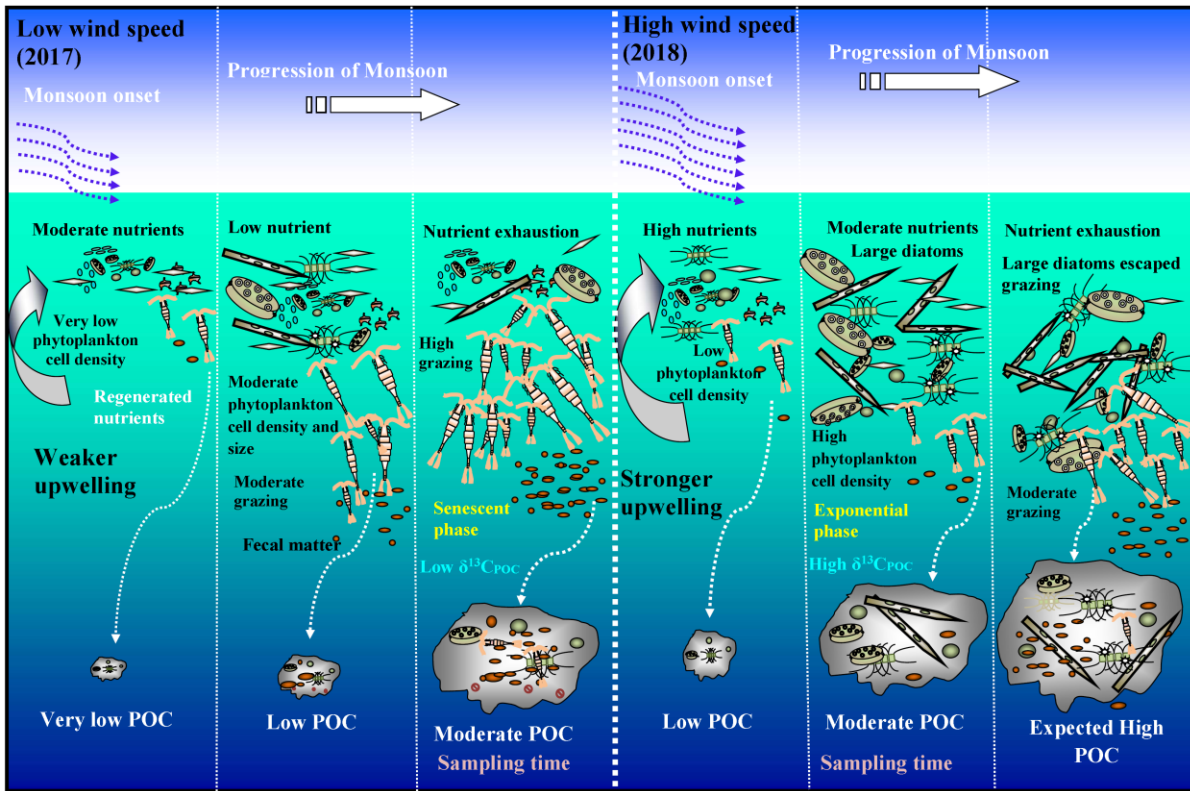


Figure 8: The correlation matrix (PAST v4.03) presenting correlations between different physicochemical and biological parameters (at significance level $p \leq 0.05$) during a) 2017 and b) 2018. The red and blue dots depict negative and positive correlations, respectively.



Not to scale

Fig. 9: Schematic representation of the phytoplankton bloom as well as particulate organic matter (POM) pool development as a consequence of upwelling emphasizing on the north of the Findlater Jet axis. Although our sampling time was the same (Aug) in 2017 and 18, the pace of POM development varied. During southwest monsoon 2017 a weaker upwelling occurred with moderate nutrient input in the euphotic zone. In 2018, the upwelling was stronger which was likely to supply higher nutrients. We hypothesize that the leftover nitrate in 2018 could potentially develop the double amount of POC observed in 2017 in the later phase of the south-west monsoon. Significantly higher $\delta^{13}C_{POC}$ values during 2018 were attributed to the early bloom phase of fast growing phytoplankton; whereas the lower values in 2017 could be due to the matured bloom phase with lower growth rate and higher zooplankton abundance.

Table 1: Average values (\pm SD; n =18 -30) and single-factor ANOVA (at level 95% confidence level) results for various parameters amongst the three regions for the years 2017 and 2018. The values marked in bold are significantly different (p value<0.05).

Parameter	North of Findlater Jet		Findlater Jet		South of Findlater Jet	
	2017	2018	2017	2018	2017	2018
POC ($\mu\text{mol L}^{-1}$)	13.08 \pm 4.01	11.71 \pm 5.62	14.93\pm3.39	7.61\pm1.82	10.31\pm3.44	7.89\pm2.21
PON ($\mu\text{mol L}^{-1}$)	2.00 \pm 0.38	1.70 \pm 0.83	2.10\pm0.48	1.25\pm0.31	1.89\pm0.58	1.25\pm0.24
C:N	6.88 \pm 2.77	6.98 \pm 0.82	7.31 \pm 1.59	6.16 \pm 1.79	5.47\pm0.82	6.26\pm0.79
$\delta^{13}\text{C}$ (‰)	-26.0\pm1.35	-25.1\pm0.7	-26.8\pm1.75	-24.6\pm0.68	-26.3\pm1.23	-24.2\pm0.29
$\delta^{15}\text{N}$ (‰)	7.68 \pm 2.60	9.24 \pm 3.03	4.94\pm1.70	6.67\pm1.79	7.48 \pm 2.96	6.62 \pm 1.34
Nitrate+nitrite ($\mu\text{mol L}^{-1}$)	2.50\pm5.17	5.26\pm4.35	3.79 \pm 1.97	4.50 \pm 1.97	1.30\pm0.98	4.05\pm1.52
DSi($\mu\text{mol L}^{-1}$)	1.48 \pm 1.35	0.92 \pm 1.37	1.74 \pm 0.61	2.16 \pm 0.98	1.49\pm0.20	2.93\pm0.96
DIP ($\mu\text{mol L}^{-1}$)	1.39\pm0.83	0.84\pm0.51	1.29 \pm 0.33	1.08 \pm 0.32	0.71\pm0.20	0.83\pm0.21
Temperature ($^{\circ}\text{C}$)	26.86\pm1.13	26.04\pm0.94	26.72\pm0.36	26.17\pm0.35	27.37\pm0.24	26.35\pm0.35
Salinity (PSU)	36.46 \pm 0.10	36.41 \pm 0.13	36.28\pm0.10	36.47\pm0.12	36.41 \pm 0.00	36.39 \pm 0.09

Supplementary Table 1: Phytoplankton cell density and zooplankton biomass recorded from the north of Findlater jet (20 °N), in the axis (18 °N) and south of it (12 °N) during 2017-2018. In 2017, considerably higher zooplankton biomass was noticed coupled with very low phytoplankton cell density and this scenario reversed in 2018.

	2017		2018	
Latitude	Phytoplankton cell density ($\times 10^3$ cells L ⁻¹)	Zooplankton biomass (ml 100 m ⁻³)	Phytoplankton cell density ($\times 10^3$ cells L ⁻¹)	Zooplankton biomass (ml 100 m ⁻³)
20 °N	4.8	348	13.1	54
18 °N	1.3	255	10.2	50
12 °N	0.4	243	9.3	47